University of Bath

Alternative formats

If you require this document in an alternative format, please contact:
openaccess@bath.ac.uk

Science
AAAS

Molecule-based metal-organic magnets with large room-temperature coercivity and critical temperature up to 242°C

Panagiota Perlepe[1,2], Itziar Oyarzabal[1,3]*, Aaron Mailman[4], Morgane Yquel[1,2], Mikhail Platunov[5,†], Iurii Dovgaliuk[6,‡], Mathieu Rouzières[1], Philippe Negrier[7], Denise Mondieig[7], Elizaveta A. Suturina[8], Marie-Anne Dourges[9], Sébastien Bonhommeau[9], Rebecca A. Musgrave[1], Kasper S. Pedersen[1,10], Dmitry Chernyshov[6], Fabrice Wilhelm[5], Andrei Rogalev[5], Corine Mathonière[2] and Rodolphe Clérac[1]*

[1] Univ. Bordeaux, CNRS, Centre de Recherche Paul Pascal, UMR 5031, F-33600, Pessac, France.
[2] CNRS, Univ. Bordeaux, Bordeaux INP, ICMCB, UMR 5026, F-33600 Pessac, France.
[3] Chemistry Faculty, University of the Basque Country, UPV/EHU, 20018, Donostia-San Sebastián, Spain.
[4] Department of Chemistry, University of Jyväskylä, P.O. Box 35, Jyväskylä, Finland.
[5] ESRF-The European Synchrotron, CS 40220, F-38043 Grenoble Cedex 9, France.
[6] Swiss-Norwegian Beamlines at the European Synchrotron Radiation Facility, F-38000 Grenoble, France.
[7] Univ. Bordeaux, CNRS, Laboratoire Ondes et Matière d'Aquitaine, UMR 5798, F-33400 Talence, France.
[8] Department of Chemistry, University of Bath, BA2 7AY, UK.
[9] Univ. Bordeaux, CNRS, Bordeaux INP, ISM, UMR 5255, F-33400 Talence, France.
[10] Department of Chemistry, Technical University of Denmark, DK-2800 Kgs. Lyngby, Denmark.

Present address:
[†] Kirensky Institute of Physics, Federal Research Center KSC SB RAS, Akademgorodok 50, bld. 38, 660036 Krasnoyarsk, Russia.
[‡] Institut des Matériaux Poreux de Paris, UMR 8004 CNRS, Ecole Normale Supérieure, Ecole Supérieure de Physique et de Chimie Industrielles de Paris, PSL Université, 75005 Paris, France.

*Corresponding authors:
Email: itziar.oyarzabal@crpp.cnrs.fr (I.O.); clerac@crpp-bordeaux.cnrs.fr (R.C.)

Abstract: 113/125 Words

Magnets derived from inorganic materials (e.g., oxides, rare earth and intermetallic compounds) are key components of modern technological applications. Despite extensive success in a broad range of applications, these inorganic magnets suffer several drawbacks, such as energetically expensive fabrication, limited availability of constituent elements, high density, and poor scope for chemical tunability. A promising design strategy for next-generation magnets relies on the versatile coordination chemistry of abundant metal ions and simple, inexpensive organic ligands. Following this approach, we report the synthesis of lightweight molecule-based magnets by post-synthetic reduction of two-dimensional coordination networks featuring chromium metal ions and pyrazine building-blocks. The resulting ferrimagnets feature critical temperatures up to 242°C, and a 7500-Oersted room-temperature coercivity.

One Sentence Summary (39/40 characters): Room-temperature molecule-based magnets

Main Text:

Magnets that operate at room temperature are usually pure metals, metal oxides, or intermetallic compounds, and find applications in numerous aspects of our daily lives. For example, magnets are key components in data processing and storage devices, are commonly employed in electrical motors that power the majority of household appliances, and are essential in renewable energy technologies (*1*). Despite their extensive use and tremendous success in technological applications, conventional magnets present several drawbacks, such as energetically expensive fabrication (e.g., SmCo and AlNiCo) and limited availability of key component elements (e.g., in lanthanide-based magnets, NdFeB and SmCo). Over the last three decades, various approaches have been developed to address these limitations and to target new engineered magnets. One particularly appealing strategy relies on the rational assembly of molecular building-blocks, such as organic ligands and paramagnetic metal ions. These molecule-based materials exhibit behavior similar to traditional magnets, but unlike the exclusively inorganic examples, they benefit from the synthetic and post-synthetic versatility resulting from the molecular and coordination chemistries, which allow precise tailoring and optimization of their properties (*2,3,4*). This synthetic approach has already led to a vast number of systems with unique magnetic behaviors, several of which have no counterpart in inorganic materials. Among these molecule-based magnets are discrete high-spin molecules known as Single-Molecule Magnets (SMMs; *5,6*), one-dimensional magnets (Single-Chain Magnets; *7*) and two- and three-dimensional (2D and 3D) networks exhibiting magnetically ordered phases (*8*). By separating magnetic metal ions with organic ligands, these molecule-based materials feature remarkably low densities (ca. 1 g cm^{-3}) compared to pure inorganic materials (generally above 5 g cm^{-3}). Although state-of-the-art inorganic magnets are indispensable due to their high maximum energy product (i.e., high magnetic density *9*), complementary molecule-based magnetic materials will be of great relevance to emergent magnetoelectronic, magnetic sensing and recording technologies as a result of their low density. However, most of these molecule-based materials suffer from low operating temperatures, which has precluded technological application.

In order to raise the operating temperature of molecule-based magnets, neutral ligands have been replaced by radicals to link paramagnetic metal ions in 2D or 3D coordination networks (*8*). The presence of a radical's spin leads to particularly strong magnetic interactions with the metal centers, which can be controlled by the chemical identity of the organic radical and metal ion, and the overlap of their magnetic orbitals containing an unpaired electron (*8,10,11*). This methodology is well exemplified by the pioneering work of J. S. Miller on a family of magnets incorporating paramagnetic metal ions and organic radical species such as the tetracyanoethylene radical ([TCNE]$^{\bullet-}$; *12*). In these systems, the strong magnetic coupling between spins localized in the metal d orbitals and those of the radicals result in magnetically ordered phases with critical temperatures (T_C) as high as 400 K (V[TCNE]$_x$, $x \sim 2$) (*13*). Apart from displaying the current record T_C value measured for a molecule-based magnet, V[TCNE]$_x$ has also shed light on the applicability of molecule-based lightweight magnets in spintronic devices, quantum information and microwave electronics (*14,15,16,17*). More recently, a new synthetic strategy was developed, subjecting pre-assembled coordination networks to post-synthetic oxidation or reduction (acting on the ligands to form radicals or metal ions to induce mixed-valency), to obtain magnetically ordered materials at a higher temperature (maximum of 105 K until this work) than their precursor (*18,19,20,21*). These combined efforts have resulted in magnets with hysteresis effects on the field (*H*) dependence of the magnetization (*M*) at ambient temperature in a small number of systems, such as TCNE-based compounds and derivatives, as well as several Prussian blue analogs

(*2,3,12,22,23*) and covalently linked organic radical frameworks (*24,25*). However, all of these molecule-based magnets have failed so far to exhibit significant room-temperature coercivity, which in the best case, is on the order of hundreds of Oersteds.

Herein, we report on the post-synthetic chemical reduction of two 2D coordination networks, $CrCl_2(pyz)_2$ and $Cr(OSO_2CH_3)_2(pyz)_2$ (pyz = pyrazine, *26,27*) in order to enhance magnetic interactions, and thus increase the critical temperature of any resulting ferrimagnetic order. While structurally similar, these two materials ($CrX_2(pyz)_2$; $X^- = [CH_3SO_3]^-$, Cl^-) exhibit contrasting physical properties. In $Cr(OSO_2CH_3)_2(pyz)_2$, the octahedral Cr^{II} metal ions are bridged by neutral, closed-shell pyrazine ligands $(pyz)°$, which transmit only weak magnetic interactions between $S = 2$ Cr^{II} spins. As a result, this material is an antiferromagnet below 10 K and an insulator (*27*). In contrast, $CrCl_2(pyz)_2$ features octahedral Cr^{III} metal ions and a mixed-valence pair of pyrazine ligands (i.e., $Cr^{III}Cl_2[(pyz)_2]^{\bullet-}$). This electronic configuration generates strong magnetic interactions between the $S = 3/2$ Cr^{III} and delocalized $S = 1/2$ pyrazine spins, leading to ferrimagnetic ordering below 55 K and a significant room-temperature electrical conductivity (*26*). In this present work, we describe the post-synthetic reduction of these 2D coordination networks, which leads to lightweight ferrimagnets with T_C up to 515 K and 7500-Oersted room-temperature coercivity.

The chemical reduction of the methanesulfonate-paired 2D material was carried out via the addition of two molar equivalents of lithium 1,2–dihydroacenaphthylenide ($Li^+[C_{12}H_{10}^{\bullet-}]$; $E_{1/2} = -3.23$ V vs. $[(C_5H_5)_2Fe]^{+/°}$; *19*) to a suspension of $Cr^{II}(OSO_2CH_3)_2(pyz)_2$ in THF (Fig. 1A, see supplementary materials for the detailed synthetic procedure; *28*). A notable color change was evident upon reduction of the light brown $Cr(OSO_2CH_3)_2(pyz)_2$ to afford product **1** as an air-sensitive, dark grey, microcrystalline powder. The powder X-ray diffraction (PXRD) pattern of **1** (Fig. S1; *28,29*) revealed a highly crystalline phase, with Bragg diffraction peaks corresponding exclusively to $Li[SO_3CH_3]$, indicating that the reduced Cr/pyrazine-containing product was either poorly crystalline, nanocrystalline or amorphous. However, the presence of THF-insoluble $Li[SO_3CH_3]$ implied that the methanesulfonate anions were partially or fully extracted from the 2D precursor upon reduction to yield a Cr-based network possibly featuring two reduced pyrazines ($[pyz]^{\bullet-}$). X-ray absorption spectroscopy (XAS) measurements at the Cr K-edge were performed on product **1**, the $Cr(OSO_2CH_3)_2(pyz)_2$ precursor containing Cr^{II} in an octahedral coordination sphere and a square-planar Cr^{II} reference complex $[Cr(N(TMS)_2)_2(py)_2]$ (noted **Cr(II)**; TMS = $Si(CH_3)_3$, py = pyridine; *30*). The X-ray absorption near-edge structure (XANES) spectrum of **1** is markedly different from that of its precursor, as well as Cr oxides and Cr metal (*31*), but its features at low energy (near-edge region) and at the Cr edge are strikingly similar to those of the square-planar **Cr(II)** reference (Fig. 1B). The near-edge structures for both product **1** and **Cr(II)**, which are the fingerprint of the Cr oxidation state in a given ligand field, show two shoulders at the same energies (~5991 and ~5994 eV). These XAS results unequivocally support that the Cr electronic structure and coordination geometry in **1** are essentially the same as in **Cr(II)**; i.e., a high-spin $S = 2$ Cr^{II} metal ion in a square-planar $\{Cr^{II}N_4\}$ environment (*30*). The structure of **1** is thus compatible with a 2D square coordination network, '$Cr^{II}(pyz^{\bullet-})_2$', reminiscent of the precursor $Cr^{II}(pyz°)_2$ layer (*27*). The field dependency of the magnetization was recorded for powder **1** at various temperatures (Fig. 1C, S2-S4; *28*), revealing broad M vs. H hysteresis loops (H_{coer} = 3400 Oe at 300 K) up to at least 400 K (the temperature limit of the MPMS magnetometer). This remarkable magnetic behavior is in sharp contrast to that reported for any known chromium-based materials (e.g., metal, nanoparticles, oxides; Table S1, *32,33,34,35,36,37,38*).
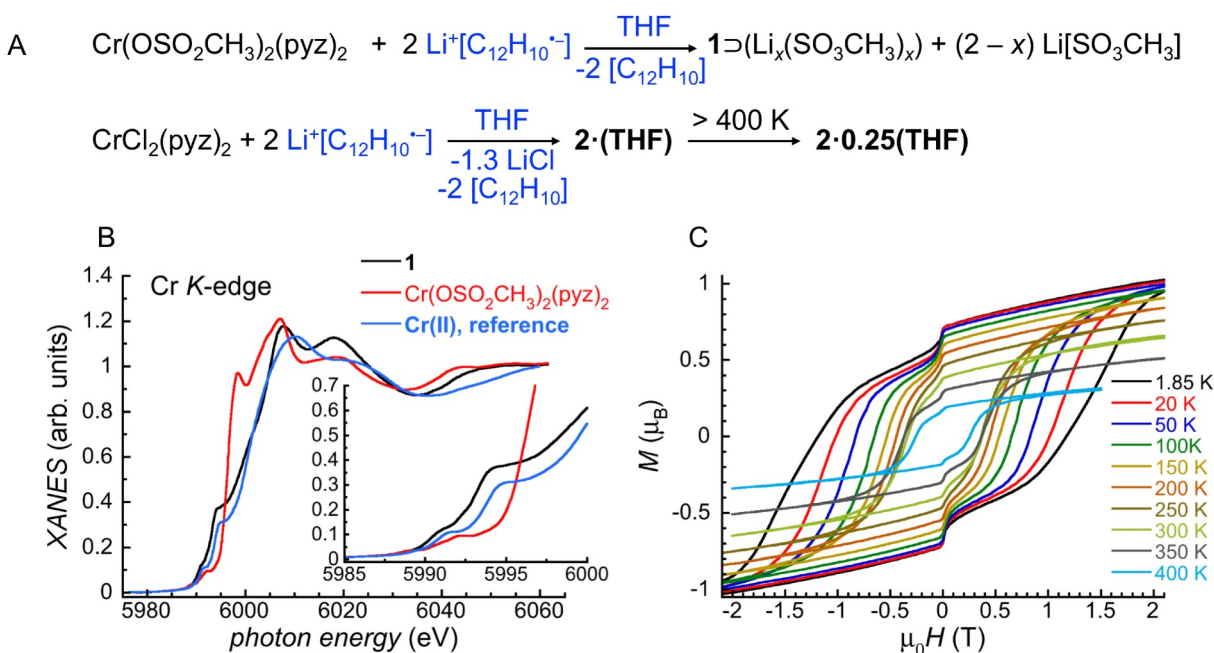
A $\quad$ $Cr(OSO_2CH_3)_2(pyz)_2$ + 2 $Li^+[C_{12}H_{10}^{\bullet-}]$ $\xrightarrow[-2\ [C_{12}H_{10}]]{THF}$ $\mathbf{1} \supset (Li_x(SO_3CH_3)_x)$ + (2 − x) $Li[SO_3CH_3]$

$CrCl_2(pyz)_2$ + 2 $Li^+[C_{12}H_{10}^{\bullet-}]$ $\xrightarrow[\substack{-1.3\ LiCl \\ -2\ [C_{12}H_{10}]}]{THF}$ $\mathbf{2 \cdot (THF)}$ $\xrightarrow{> 400\ K}$ $\mathbf{2 \cdot 0.25(THF)}$

Fig. 1. Chemical reduction of $Cr(OSO_2CH_3)_2(pyz)_2$ and $CrCl_2(pyz)_2$. (**A**) Reaction schemes (solvents and soluble species in blue; solid materials in black; the ⊃ symbol indicates the presence of $Li_x(SO_3CH_3)_x$ within **1**). (**B**) Normalized XANES spectra at the Cr *K*-edge region of **1** (black trace), $Cr(OSO_2CH_3)_2(pyz)_2$ (red trace) and **Cr(II)** reference (blue trace) at 295 K. Inset: magnified view of the near-edge region. (**C**) Magnetization versus applied *dc* magnetic field data (at 7 Oe s^{-1}) in the −2.1 to 2.1 T field range for **1** between 1.85 and 400 K. As the exact composition of **1** is unknown, the magnetization data were normalized using the molecular weight of the $Cr(OSO_2CH_3)_2(pyz)_2$ parent compound.

Hence, the above experimental evidence unequivocally confirms that the post-synthetic chemical reduction of $Cr^{II}(OSO_2CH_3)_2(pyz)_2$ resulted in a mixture of insoluble crystalline $Li[SO_3CH_3]$ and an amorphous '$Cr^{II}(pyz^{\bullet-})_2$' phase, which displayed remarkable hard magnet properties (H_{coer} = 3400 Oe at 300 K), and a critical temperature above 400 K. In order to target a pure analog of this room-temperature magnet, our focus turned to the related $CrCl_2(pyz)_2$ system, which is expected to yield the same magnetic material upon reduction of both the pyrazine scaffold ($[(pyz)_2]^{\bullet-} \rightarrow$ $(pyz^{\bullet-})_2$) and the Cr^{III} metal ion ($Cr^{III} \rightarrow Cr^{II}$). More importantly, the anticipated byproduct of this reaction, LiCl (Fig. 1A), should be far easier to remove from the Cr-based product than $Li[SO_3CH_3]$ due to its increased solubility in organic media, particularly THF. Using identical experimental conditions to those for the synthesis of **1**, the $CrCl_2(pyz)_2$ precursor was exposed to $Li^+[C_{12}H_{10}^{\bullet-}]$ (Fig. 1A, *28*). Synchrotron PXRD experiments on the resulting dark grey solid (90% isolated yield), revealed several prominent diffraction peaks and, notably, the absence of an independent crystalline LiCl phase (Fig. S5, *28*). The diffractogram was refined in the orthorhombic *Pmmm* space group with the following cell parameters: a = 6.9239(9), b = 6.9524(2) and c = 8.478(2) Å (V = 408.1(1) Å^3). It is worth noting that the a and b lattice parameters obtained for this material (noted **2·(THF)** herein) are close to those found in the $CrCl_2(pyz)_2$ precursor (*Immm* space group*: a = 6.90351(4), b = 6.97713(4) and c = 10.82548(6) Å; V = 521.427(6) Å^3; ρ

= 1.803 g cm^{-3}). This suggests the presence of a similar 2D Cr(pyz)$_2$-type network in both CrCl$_2$(pyz)$_2$ and **2·(THF)**.

The Cr K-edge XANES spectra of **2·(THF)** is remarkably similar to that of both the model square-planar complex **Cr(II)** and **1** (Fig. 1B), while clearly different to that of the precursor Cr^{III}Cl$_2$(pyz)$_2$ (Fig. 2A). Therefore, we conclude that the reduction of CrCl$_2$(pyz)$_2$ results in the reduction of octahedral high-spin Cr^{III} metal ions into square-planar high-spin Cr^{II} sites, implying the loss of both axial chloride ligands in **2·(THF)**. Raman spectroscopy further supports this conclusion, as evidenced by the absence of the characteristic Cr–Cl symmetric stretching band (ca. 260 cm^{-1}), while the position and narrow nature of Raman bands in the pyrazine fingerprint region of the spectrum (600–1700 cm^{-1}) suggest the presence of only reduced [pyz]$^{\bullet-}$ ligands (Fig. S6-S7, Tables S2-S4, *28*). In order to understand the reduction mechanism and the concomitant chloride decoordination, quantum chemical geometry optimizations were performed on [CrCl$_x$(pyz)$_4$]$^{2-x-q}$ molecular fragments (where the number of chloride ligands, x = 2, 1, 0; and successive reductions are represented by q = 0, 1, 2, 3 or 4; Table S5, *28*). Upon addition of 4 electrons to the initial [CrCl$_2$(pyz)$_4$]^0 fragment, the calculations show a minimum energy at infinite Cr···Cl distance, indicating the instability of the fully reduced bis-chloride-bound fragment, [CrCl$_2$(pyz)$_4$]$^{4-}$. Upon removal of chloride anions, the ability of the [CrCl(pyz)$_4$]$^+$ and [Cr(pyz)$_4$]$^{2+}$ fragments to stabilize reduced pyrazine ligands increases around the Cr^{II} center (Fig. S8, *28*). The pyrazine reduction is thus facilitated by the chloride dissociation. Moreover, the optimized structure of the [Cr(pyz)$_4$]$^{2-}$ fragment (q = 4, pyrazines are all reduced around the Cr^{II} center) adopts a perfect square-planar geometry (Table S5, *28*), which makes this moiety ideal for forming extended Cr(pyz)$_2$-type sheets.
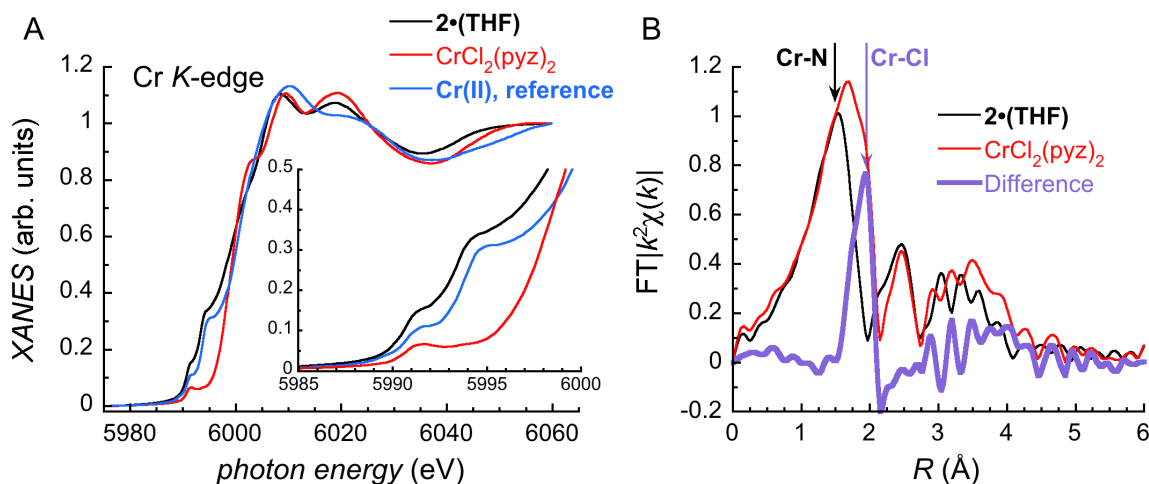

Fig. 2. XANES and EXAFS spectra at the Cr K-edge at 295 K. (**A**) Normalized XANES spectra of **2·(THF)** (black trace), CrCl$_2$(pyz)$_2$ (red trace) and **Cr(II)** reference (blue trace). Inset: magnified view of the near-edge region. (**B**) Fourier-transform (FT) EXAFS spectra for **2·(THF)** (black trace) and CrCl$_2$(pyz)$_2$ (red trace; see Figs. S9-S10 for additional EXAFS data, *28*). The difference of the two data sets is shown in purple.

A comparison of the extended X-ray absorption fine structure (EXAFS) at the Cr K-edge of **2·(THF)** and its precursor provides further experimental evidence for chloride decoordination. As shown in Fig. 2B, the Fourier-transform EXAFS spectra of CrCl$_2$(pyz)$_2$ and **2·(THF)** are similar

except at $R \sim 1.9$ Å, where a significant difference is evident (see Figs. S9-S10 for EXAFS and k^2-weighted EXAFS spectra; *28*). This corresponds to a major modification in the local environment of the Cr^{II} site. In the precursor compound, $CrCl_2(pyz)_2$, the broad feature at $R = 1.67$ Å and the shoulder at 1.91 Å can be attributed to the Cr–N (2.003-2.059 Å) and Cr–Cl (2.337 Å) bonds, respectively. However, while the Cr–N bond in **2·(THF)** is found at $R = 1.53$ Å, the signature of the Cr–Cl bond around $R \sim 1.9$ Å is significantly attenuated (see difference spectrum, Fig. 2B), corroborating the loss of axial Cl^- ions and the resulting square planar geometry at the Cr center.

Combustion elemental analysis (EA) and inductively coupled plasma-optical emission spectroscopy (ICP-OES) measurements support the above assumptions and reveal the presence of 0.7(1) Li ion and 0.99(6) THF molecule per $Cr(pyz)_2$ moiety, each assumed to reside between the $Cr^{II}(pyz^{\bullet-})_2$ layers in **2·(THF)** (Table S6, *28*). In addition, XANES measurements at the Cl K-edge for $CrCl_2(pyz)_2$ and **2·(THF)** provide evidence for remaining chlorine anions (ca. 0.7 per Cr) in the reduced material (Fig. S11, *28*). The near-edge feature, which corresponds to a transition from the Cl $1s$ orbital to molecular orbitals of hybridized Cl $3p$ and Cr $3d$ states in Cr/Cl complexes (*26*), is much lower in intensity in the spectrum of **2·(THF)** versus its precursor. This feature reflects a considerable weakening of the chromium-chloride interaction and subsequent elongation of the Cr$\cdots$Cl distance (i.e., decoordination from the Cr metal ion; *39*) in **2·(THF)**, which corroborates the theoretical XANES calculations (Fig. S12, *28*) and experimental EXAFS data (Figs. 2B, S9-S10, *28*). However, the presence of a detectable near-edge signal indicates that chloride ions are still close enough to the Cr^{II} ions in order to interact electronically (see a comparison with LiCl in Fig. S13 in which Li^+ and Cl^- ions are ionically independent, *28*). To summarize, **2·(THF)** is a material possessing neutral 2D $Cr^{II}(pyz^{\bullet-})_2$ layers of square planar Cr^{II} metal ions and two singly reduced pyrazines, separated by one THF molecule and 0.7(1) equivalents of Li^+ and Cl^- ions. The chemical formula of **2·(THF)** can therefore be defined as $Li_{0.7}[Cr(pyz)_2]Cl_{0.7}\cdot(THF)$ (with a calculated density of 1.278 g cm^{-3}).

Variable-temperature PXRD measurements on **2·(THF)** revealed an irreversible phase transformation upon heating above 380 K (Fig. S14, *28*). This new phase is stable up to 500 K and remains the sole phase upon cooling to room temperature. As evidenced by thermogravimetric analysis - mass spectrometry measurements (TGA-MS, Figs. S15-S20, *28*), this irreversible structural change is due to a loss of the interlayer THF molecules. Fourier-transform infrared spectroscopy (FTIR, Figs. S21-S24, *28*) and EA measurements on samples of **2·(THF)** after prolonged heating (18 hours at 400 K or 10 hours at 500 K) however show a residual presence of about 0.25 THF per formula unit, in good agreement with TGA-MS measurements (Fig. S17, Table S6, *28*). XANES measurements at the Cr K-edge of this heat-treatment product, **2·0.25(THF)**, indicated no significant change in the Cr^{II} coordination environment upon partial THF loss (Fig. S25, *28*). On the other hand, the Cl K-edge spectrum showed an attenuation in the near-edge region versus **2·(THF)** (Fig. S26, *28*), indicating reduced mixing between Cl $3p$ and Cr $3d$ orbitals; i.e., greater localization of Cl p states. The chlorine anions are thus slightly further from the Cr ions after the partial loss of the interlayer THF molecules. The diffractogram of **2·0.25(THF)** is less affected than that of **2·(THF)** by the anisotropic broadening of the diffraction peaks systematically associated with planes possessing a non-zero l Miller index (Figs. 3A, S14 and S27, *28*). For both compounds, this observation implies less crystallographic order along the c direction (and thus in the spacing between the sheets) than within the ab plane of the 2D network as is expected for layered materials (*40,41*). The diffractogram of **2·0.25(THF)** at 290 K was fully indexed in the tetragonal $P4/mmm$ space group with $a = b = 6.9893(1)$ and $c = 7.195(3)$ Å ($V =$

351.5(1) Å^3; ρ = 1.228 g cm^{-3}; Fig. 3A, Table S7, *28*) showing that upon removing the THF molecules, the inter-layer distance diminishes significantly, as evidenced by the decrease of the c parameter from ~8.5 in **2·(THF)** to ~7.2 Å in **2·0.25(THF)** (for comparison the inter-layer distance in the CrCl$_2$(pyz)$_2$ precursor is 5.4 Å).
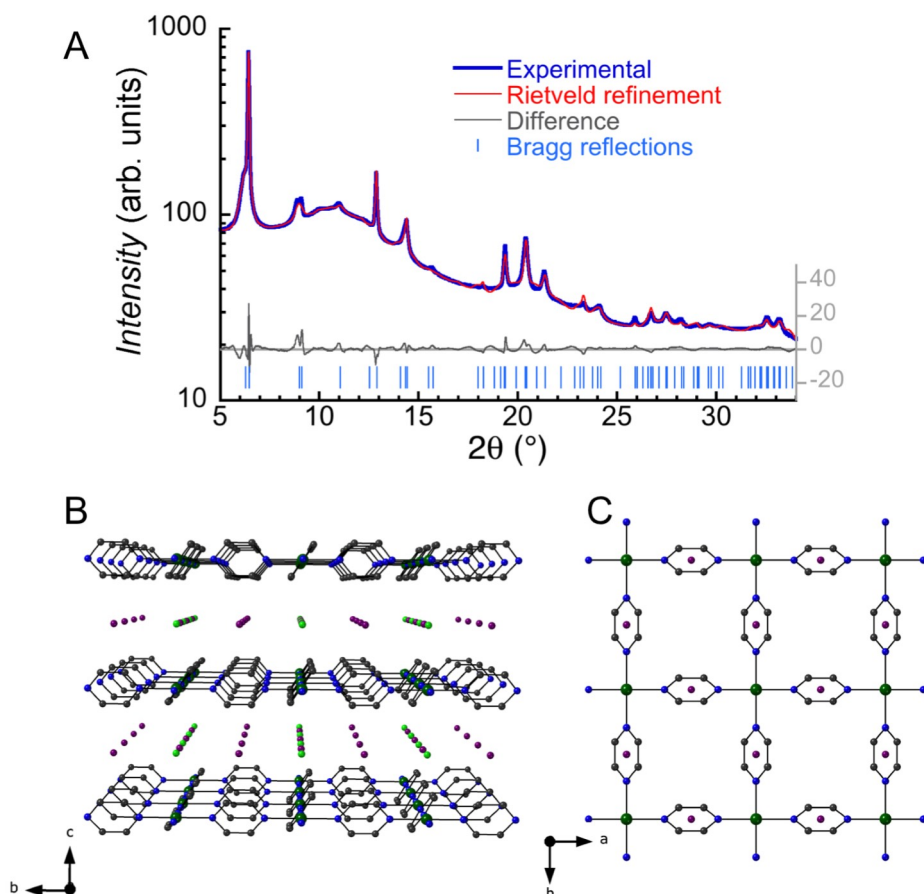
Fig. 3. Structural model of Li$_{0.7}$[Cr(pyz)$_2$]Cl$_{0.7}$·0.25(THF) (2·0.25(THF)). (**A**) The best Rietveld refinement (red trace; R_I = 4.23 %) of the synchrotron PXRD pattern of **2·0.25(THF)** at 290 K (after cooling from 500 K in a sealed capillary; blue trace) is shown together with the experimental/model difference (grey trace) and calculated Bragg reflections (blue bars). (**B**) Perspective view (along the a direction) of **2·0.25(THF)** showing the alternation of {Li$_{0.7}$Cl$_{0.7}$} and neutral Cr^{II}(pyz$^{•-}$)$_2$ layers stacking along the c direction. (**C**) Eclipsed layered structure viewed along the c direction. Cr: dark green, N: blue, C: black. Cl (light green) and Li (purple) are shown at a fixed occupancy of 70% according to the elemental composition. Hydrogen atoms have been omitted for clarity.

Considering all the above information, an appropriate structural model was used to refine the experimental PXRD pattern obtained for **2·0.25(THF)**, yielding reasonable agreement factors (e.g., R_I = 4.23 %, R_p = 1.63 % and R_{wp} = 2.32 % at 290 K, Fig. 3, Table S7, *28*). As expected, the Cr sites in **2·0.25(THF)** are bridged by pyrazine ligands forming a 2D square Cr(pyz)$_2$ network in the crystallographic ab plane. In contrast to the precursors CrCl$_2$(pyz)$_2$ and Cr(OSO$_2$CH$_3$)$_2$(pyz)$_2$

(*26, 27*), these $Cr(pyz)_2$ layers in **2·0.25(THF)** are eclipsed along the *c* direction (Fig. 3C). The square-planar coordination sphere of Cr is occupied by four nitrogen atoms from four pyz ligands, with a Cr–N distance of 2.0440(6) Å. As evidenced by other techniques on **2·THF** and **2·0.25(THF)** (*vide supra*), the Cl⁻ anions are not coordinated to the Cr metal ions, but are located in between Cr sites of two adjacent layers with a Cr···Cl distance of 3.598(2) Å. Within this structural model, it was not possible to localize THF molecules, but the Li cations are most likely positioned in between pyrazines for electrostatic reasons and slightly better refinement of the PXRD data.

The magnetic properties of **2·(THF)** were studied and compared with those collected for **1** (Figs. S2-S4; *28*). Zero-field cooled (ZFC)/field-cooled (FC) magnetization data were collected under a *dc* field of 50 Oe for a sample of **2·(THF)** (and thus for **2·0.25(THF)** after partial desolvation from ca. 400 K onwards) on a Microsense Vibrating Sample Magnetometer (VSM) capable of reaching temperatures up to 600 K. The magnetization bifurcation point of the ZFC/FC data, which corresponds to the temperature at which the coercive field vanishes, is found at ~510 K (Fig. 4A). This temperature agrees well with the *M* vs. *H* curves, which show a crossover between *S*-shape and linear (typical of a paramagnetic state) forms between 510 and 520 K (Fig. 4B-C). As also confirmed by the vanishing of the remnant magnetization at 510 K (Fig. 4D), the critical temperature of **2·0.25(THF)** is thus ~510 K, exceeding by ~110 K the ordering temperature measured for $V[TCNE]_x$ (*13*). It is worth emphasizing that the linear dependence of the magnetization at 520 K after the disappearance of the *M* vs. *H* hysteresis loops rules out the presence of any superparamagnetic nanoparticles. Upon cooling from 520 K to room temperature, the *M* vs. *H* hysteresis loops are recovered as expected for a phase transition between paramagnetic and ferri-/ferromagnetic states. Nevertheless, the absolute value of the magnetization is systematically lower than during the heating process (Figs. S28-S29, *28*), suggesting that the critical temperature of **2·0.25(THF)** is in close proximity to its decomposition temperature under the experimental conditions of the magnetic measurements (i.e., in a sealed quartz tube under inert atmosphere). Similar to the powder **1** (Fig. 1C, S2-S4, *28*), **2·(THF)** is a hard magnet with a remarkably large coercive field of 5300 Oe at room temperature (13500 Oe at 1.85 K; Figs. 4B-C and S30, *28*). This value compares well with those of widely used inorganic magnets and is larger than any of those observed for molecule-based magnets (which are on the order of hundreds of Oersteds in the best cases; Table S8, *28*). The coercive field reproducibly displays an anomalous increase at ca. 350 K on the initial heating of **2·(THF)** (Fig. S30, *28*) and **1** (Fig. S4, *28*) samples, while no such feature is observed in the remnant magnetization, shown in Figs. 4D, S29 and S3 (*28*). This anomaly of the coercive field, which is absent in measurements on **2·0.25(THF)** (prepared by annealing **2·(THF)**; Figs. S30-S35, *28*), is thus likely linked to the partial loss of interlayer THF around 300-400 K (*vide supra*) and the associated irreversible structural rearrangement (Fig. S14, *28*). Indeed, the magnetic properties (magnetization and X-ray spectroscopy measurements; Fig. S36-S37) of **2·(THF)** and **2·0.25(THF)** samples are similar, with only slight variation in T_C (510 K vs. 515 K respectively), but a noticeable 50% difference in the coercivity at 300 K (5300 Oe vs. 7500 Oe respectively; Figs. 4C, S32 and S37, *28*). These results show that the annealing of **2·(THF)** to remove most of the THF molecules, significantly improves the T_C and H_{coer} characteristics of the resulting magnet, **2·0.25(THF)**.
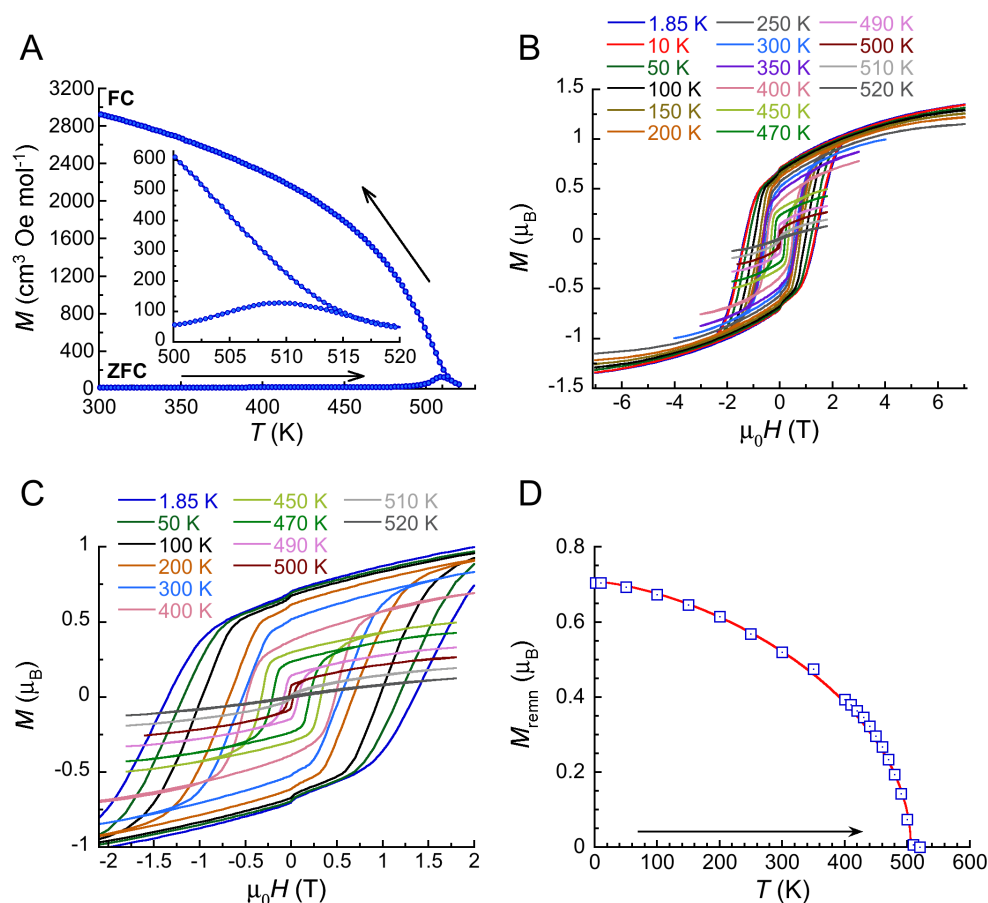
Fig. 4. Magnetic properties of 2·(THF) and 2·0.25(THF) (after partial desolvation above 400 K). (**A**) Zero field-cooled (ZFC)/field-cooled (FC) magnetization data obtained under an applied *dc* magnetic field of 50 Oe at 5 K min^{-1}. Inset: magnified view of the main plot in the 500–520 K temperature range. The solid lines are a guide for the eye. (**B**) Magnetization versus applied *dc* magnetic field data (at 5 to 12 Oe s^{-1}) in the −7 to 7 T field range, from 1.85 K to 520 K. (**C**) Magnified view of selected data from Fig. 4B in the −2 to 2 T field range. (**D**) Temperature dependence of the remnant magnetization, M_{remn}, determined from the *M* vs. *H* data from 1.85 K to 520 K (Figs. 4B-C). The solid red line is the best fit to the mean-field (MF) Bloch law: $M_{remn} \propto (1 − (T/T_{C-MF})^{3/2})^{1/2}$ with T_C = 506 K (considering data up to 490 K, χ^2(GoF) = 0.00057; *42*).

At 1.85 K, the magnetization of both **2·(THF)** and **2·0.25(THF)** does not saturate at 7 T, but reproducibly reaches a maximum value of 1.34 μ_B (Figs. 4B and S31, *28*). This value is significantly lower than that of 2 μ_B predicted for an ordered ferrimagnetic state with antiferromagnetically coupled spins (one S = 2 Cr^{II} center and two S = ½ pyrazine radicals; assuming *g*-factors of 2). In an analogous manner to CrCl$_2$(pyz)$_2$ (*26*), the low magnetization may originate from the high degree of conjugation between the Cr *d* orbitals and pyrazine π states, which leads to a partial delocalization of the Cr spin density over the organic scaffold, and strong Cr-radical antiferromagnetic interactions. As evidenced by single-point broken-symmetry calculations performed on a [Cr(pyz)$_4$]$^{2−}$ fragment taken from the **2·0.25(THF)** structural model (Figs. 3B-C), the Cr-radical exchange coupling is strongly antiferromagnetic and ranges from

-336 to -429 cm^{-1} (-483 to -617 K with the $-2J$ convention) depending on the tilting of the radical pyrazines (Tables S9-S10, Fig. S38, *28*). These strong antiferromagnetic interactions are in perfect agreement with the ferrimagnetic order experimentally observed at high temperature for these materials.

This work reports molecule-based metal-organic magnets with high critical temperature up to 515 K and large room-temperature coercivity, which compete well with the characteristics of the traditional inorganic magnets and surpass the properties of previously known molecule-based magnets (Table S8, *28*). We show that the post-synthetic chemical reduction of coordination networks is a general, simple and efficient synthetic approach that offers broad perspectives for the preparation of a completely new generation of high-temperature lightweight magnets, with yet unrealized application in emergent technologies. Finally, it should be highlighted that the reduced materials reported in this study are electrically insulating (as expected due to the absence of mixed-valency), while the mixed-valence $[Cr^{III}Cl_2(pyz_2)^{\bullet-}]$ precursor shows a significant room-temperature conductivity of 32 mS cm^{-1} (*26*). Therefore, exciting potential exists in fine-tuning the post-synthetic reduction of these 2D coordination materials, leading to the further development of new high-T_C conducting molecule-based magnets.

References and Notes:

1. O. Gutfleisch, M. A. Willard, E. Brück, C. H. Chen, S. G. Sankar, J. P. Liu, Magnetic materials and devices for the 21st century: stronger, lighter, and more energy efficient. *Adv. Mater.* **23**, 821-842 (2011).
2. J. S. Miller, Organic- and molecule-based magnets. *Mater. Today* **17**, 224-235 (2014).
3. J. S. Miller, Magnetically ordered molecule-based materials. *Chem. Soc. Rev.* **40**, 3266-3296 (2011).
4. O. Kahn, *Molecular Magnetism* (VCH, Weinheim, 1993).
5. D. Gatteschi, R. Sessoli, J. Villain, *Molecular Nanomagnets* (Oxford University Press, 2006).
6. S. Demir, I.-R. Jeon, J. R. Long, T. D. Harris, Radical ligand-containing single-molecule magnets. *Coord. Chem. Rev.* **289-290**, 149-176 (2015).
7. C. Coulon, V. Pianet, M. Urdampilleta, R. Clérac, Single-Chain Magnets and Related Systems. In *Molecular Nanomagnets and Related Phenomena. Structure and Bonding,* S. Gao Eds. (Springer, Berlin, Heidelberg, 2014), vol. 164, pp. 143-184.
8. A. E. Thorarinsdottir, T. D. Harris, Metal-organic framework magnets. *Chem. Rev.* 10.1021/acs.chemrev.9b00666 (2020).
9. J. M. D. Coey, *Magnetism and Magnetic Materials* (Cambridge University Press, Cambridge, 2010).
10. N. Motokawa, H. Miyasaka, M. Yamashita, K. R. Dunbar, An electron-transfer ferromagnet with T_C = 107 K based on a three-dimensional [Ru$_2$]$_2$/TCNQ system. *Angew. Chem. Int. Ed.* **47**, 7760-7763 (2008).
11. X. Ma, E. A. Suturina, S. De, P. Négrier, M. Rouzières, R. Clérac, P. Dechambenoit, A redox-active bridging ligand to promote spin delocalization, high-spin complexes, and magnetic multi-switchability. *Angew. Chem. Int. Ed.* **57**, 7841-7845 (2018).
12. J. S. Miller, S.-I. Ohkoshi, High-T_C Ordered Molecular Magnets. In *Molecular Magnetic Materials: Concepts and Applications,* B. Sieklucka, D. Pinkowicz, Eds. (Wiley-VCH, 2017), chap. 7.

13. J. M. Manriquez, G. T. Yee, R. S. Mclean, A. J. Epstein, J. S. Miller, A room-temperature molecular/organic-based magnet. *Science* **252**, 1415-1417 (1991).

14. H. Liu, C. Zhang, H. Malissa, M. Groesbeck, M. Kavand, R. McLaughlin, S. Jamali, J. Hao, D. Sun, R. A. Davidson, L. Wojcik, J. S. Miller, C. Boehme, Z. V. Vardeny, Organic-based magnon spintronics. *Nat. Mater.* **17**, 308-312 (2018).

15. N. Zhu, X. Zhang, I. H. Froning, M. E. Flatté, E. Johnston-Halperin, H. X. Tang, Low loss spin wave resonances in organic-based ferrimagnet vanadium tetracyanoethylene thin films. *Appl. Phys. Lett.* **109**, 082402 (2016).

16. M. Chilcote, M. Harberts, B. Fuhrmann, K. Lehmann, Y. Lu, A. Franson, H. Yu, N. Zhu, H. Tang, G. Schmidt, E. Johnston-Halperin, Spin-wave confinement and coupling in organic-based magnetic nanostructures. *APL Mater.* **7**, 111108 (2019).

17. A. Franson, N. Zhu, S. Kurfman, M. Chilcote, D. R. Candido, K. S. Buchanan, M. E. Flatté, H. X. Tang, E. Johnston-Halperin, Low-damping ferromagnetic resonance in electron-beam patterned, high-Q vanadium tetracyanoethylene magnon cavities. *APL Mater.* **7**, 121113 (2019).

18. K. Taniguchi, J. Chen, Y. Sekine, H. Miyasaka, Magnetic phase switching in a tetraoxolene-bridged honeycomb ferrimagnet using a lithium ion battery system. *Chem. Mater.* **29**, 10053-10059 (2017).

19. L. Liu, J. A. DeGayner, L. Sun, D. Z. Zee, T. D. Harris, Reversible redox switching of magnetic order and electrical conductivity in a 2D manganese benzoquinoid framework. *Chem. Sci.* **10**, 4652-4661 (2019).

20. J. A. DeGayner, I.-R. Jeon, L. Sun, M. Dincă, T. D. Harris, 2D conductive iron-quinoid magnets ordering up to $T = 105$ K via heterogenous redox chemistry. *J. Am. Chem. Soc.* **139**, 4175-4184 (2017).

21. L. E. Darago, M. L. Aubrey, C. J. Yu, M. I. Gonzalez, J. R. Long, Electronic conductivity, ferrimagnetic ordering, and reductive insertion mediated by organic mixed-valence in a ferric semiquinoid metal-organic framework. *J. Am. Chem. Soc.* **137**, 15703-15711 (2015).

22. J. S. Miller, Oliver Kahn lecture: composition and structure of the V[TCNE]$_x$ (TCNE = tetracyanoethylene) room-temperature, organic-based magnet - a personal perspective. *Polyhedron* **28**, 1596-1605 (2009).

23. S. Ferlay, T. Mallah, R. Ouahès, P. Veillet, M. Verdaguer, A room-temperature organometallic magnet based on Prussian blue. *Nature* **378**, 701-703 (1995).

24. J. Mahmood, J. Park, D. Shin, H.-J. Choi, J.-M. Seo, J.-W. Yoo, J.-B. Baek, Organic ferromagnetism: trapping spins in the glassy state of an organic network structure. *Chem* **4**, 2357-2369 (2018).

25. H. Phan, T. S. Herng, D. Wang, X. Li, W. Zeng, J. Ding, K. P. Loh, A. T. S. Wee, J. Wu, Room-temperature magnets based on 1,3,5-triazine-linked porous organic radical frameworks. *Chem* **5**, 1223-1234 (2019).

26. K. S. Pedersen, P. Perlepe, M. L. Aubrey, D. N. Woodruff, S. E. Reyes-Lillo, A. Reinholdt, L. Voigt, Z. Li, K. Borup, M. Rouzières, D. Samohvalov, F. Wilhelm, A. Rogalev, J. B. Neaton, J. R. Long, R. Clérac, Formation of the layered conductive magnet CrCl$_2$(pyrazine)$_2$ through redox-active coordination chemistry. *Nat. Chem.* **10**, 1056-1061 (2018).

27. P. Perlepe, I. Oyarzabal, K. S. Pedersen, P. Negrier, D. Mondieig, M. Rouzières, E. A. Hillard, F. Wilhelm, A. Rogalev, E. A. Suturina, C. Mathonière, R. Clérac, Cr(pyrazine)$_2$(OSO$_2$CH$_3$)$_2$: a two-dimensional coordination polymer with an antiferromagnetic ground state. *Polyhedron* **153**, 248-253 (2018).

28. See supplementary materials.

29. T. Trella, W. Frank, poster presented at the 17. Conference of the GDCh Division of Solid State Chemistry and Materials Research, Dresden, DE, 15-17 September 2014.

30. Y.-F. Deng, T. Han, Z. Wang, Z. Ouyang, B. Yin, Z. Zheng, J. Krzystek, Y.-Z- Zheng, Uniaxial magnetic anisotropy of square-planar chromium(II) complexes revealed by magnetic and HF-EPR studies. *Chem. Commun*. **51**, 17688-17691 (2015).

31. S. Cuello, J. Entwisle, J. Benning, C. Liu, S. Coburn, K. G. McAdam, J. Braybrook, H. Goenaga-Infante, Complementary HPLC-ICP-MS and synchrotron X-ray absorption spectroscopy for speciation analysis of chromium in tobacco samples. *J. Anal. At. Spectrom*. **31**, 1818-1829 (2016).

32. E. Fawcett, Spin-density-wave antiferromagnetism in chromium. *Rev. Mod. Phys*. **60**, 209-283 (1988).

33. C. G. Shuli, M. K. Wilkinson, Neutron diffraction studies of various transition elements. *Rev. Mod. Phys*. **25**, 100-107 (1953).

34. G. E. Bacon, N. Cowlam, Magnetic studies of annealed and alloyed chromium by neutron diffraction. *J. Phys. C: Solid State Phys*. **2**, 238-251 (1969).

35. T. Furubayashi, I. Nakatani, Curie paramagnetism of chromium ultrafine particles. *J. Appl. Phys*. **73**, 6412-6413 (1993).

36. W. Abdul-Razzaq, M. S. Seehra, Observation of oxidation and mechanical strain in Cr nanoparticles produced by ball-milling. *Phys. Stat. Sol*. **193**, 94-102 (2002).

37. S. Foner, High-field antiferromagnetic resonance in Cr_2O_3. *Phys. Rev*. **130**, 183-197 (1963).

38. J. M. D. Coey, M. Venkatesan, Half-metallic ferromagnetism: example of CrO_2. *J. Appl. Phys*. **91**, 8345-8350 (2002).

39. S. DeBeer George, P. Brant, E. I. Solomon, Metal and ligand K-edge XAS of organotitanium complexes: metal 4p and 3d contributions to pre-edge intensity and their contributions to bonding. *J. Am. Chem. Soc*. **127**, 667-674 (2005).

40. A. B. Cairns, A. L. Goodwin, Structural disorder in molecular framework materials. *Chem. Soc. Rev*. **42**, 4881-4893 (2013).

41. T. N. Ramesh, R. S. Jayashree, P. V. Kamath, Disorder in layered hydroxides: DIFFaX simulation of the X-ray powder diffraction patterns of nickel hydroxide. *Clays Clay Miner*. **51**, 570-576 (2003).

42. R. Skomski, Permanent Magnets: History, Current Research, and Outlook. In *Novel Functional Magnetic Materials. Springer Series in Materials Science*, A. Zhukov Ed. (Springer Series in Materials Science, 2016), vol. 231, pp. 359-395.

43. F. Neese, Software update: the ORCA program system, version 4.0. *WIREs Comp. Mol. Sci*. **8**, e1327 (2018).

44. F. Neese, The ORCA program system. *WIREs Comp. Mol. Sci*. **2**, 73-78 (2012).

45. A. D. Becke, A new mixing of Hartree-Fock and local density-functional theories. *J. Chem. Phys*. **98**, 1372-1377 (1993).

46. C. Lee, W. Yang, R. G. Parr, Development of the Colle-Salvetti correlation-energy formula into a functional of the electron density. *Phys. Rev. B* **37**, 785-789 (1988).

47. S. H. Vosko, L. Wilk, M. Nusair, Accurate spin-dependent electron liquid correlation energies for local spin density calculations: a critical analysis. *Can. J. Phys*. **58**, 1200-1211 (1980).

48. P. J. Stephens, F. J. Devlin, C. F. Chabalowski, M. J. Frisch, Ab Initio calculation of vibrational absorption and circular dichroism spectra using density functional force fields. *J. Phys. Chem*. **98**, 11623-11627 (1994).

49. F. Weigend, R. Ahlrichs, Balanced basis sets of split valence, triple zeta valence and quadruple zeta valence quality for H to Rn: Design and assessment of accuracy. *Phys. Chem. Chem. Phys.* **7**, 3297-3305 (2005).

50. M. J. Frisch, G. W. Trucks, H. B. Schlegel, G. E. Scuseria, M. A. Robb, J. R. Cheeseman, G. Scalmani, V. Barone, G. A. Petersson, H. Nakatsuji, M. C. X. Li, A. Marenich, J. Bloino, B. G. Janesko, R. Gomperts, B. Mennucci, H. P. Hratchian, J. V. Ortiz, A. F. Izmaylov, J. L. Sonnenberg, D. Williams-Young, F. Ding, F. Lipparini, F. Egidi, J. Goings, B. Peng, A. Petrone, T. Henderson, D. Ranasinghe, V. G. Zakrzewski, N. R. J. Gao, G. Zheng, W. Liang, M. Hada, M. Ehara, K. Toyota, R. Fukuda, J. Hasegawa, M. Ishida, T. Nakajima, Y. Honda, O. Kitao, H. Nakai, T. Vreven, K. Throssell, J. A. M. Jr., J. E. Peralta, F. Ogliaro, M. Bearpark, J. J. Heyd, E. Brothers, K. N. Kudin, V. N. Staroverov, T. Keith, R. Kobayashi, J. Normand, K. Raghavachari, A. Rendell, J. C. Burant, S. S. Iyengar, J. Tomasi, M. Cossi, J. M. Millam, M. Klene, C. Adamo, R. Cammi, J. W. Ochterski, R. L. Martin, K. Morokuma, O. Farkas, J. B. Foresman, D. J. Fox, Gaussian, Revision D.01 (Gaussian, Inc., Wallingford, CT, 2016).

51. N. Lee, T. Petrenko, U. Bergmann, F. Neese, S. DeBeer, Probing valence orbital composition with iron k$_\beta$ X-ray emission spectroscopy. *J. Am. Chem. Soc.* **132**, 9715-9727 (2010).

52. A. D. Becke, Density-functional exchange-energy approximation with correct asymptotic behavior. *Phys. Rev. A* **38**, 3098-3100 (1988).

53. J. P. Perdew, Density-functional approximation for the correlation energy of the inhomogeneous electron gas. *Phys. Rev. B* **33**, 8822-8824 (1986).

54. D. A. Pantazis, X.-Y. Chen, C. R. Landis, F. Neese, All-electron scalar relativistic basis sets for third-row transition metal atoms. *J. Chem. Theory Comput.* **4**, 908-919 (2008).

55. F. Neese, Efficient and accurate approximations to the molecular spin-orbit coupling operator and their use in molecular *g*-tensor calculations. *J. Chem. Phy.* **122**, 034107 (2005).

56. B. de Souza, G. Farias, F. Neese, R. Izsák, Predicting phosphorescence rates of light organic molecules using time-dependent density functional theory and the path integral approach to dynamics. *J. Chem. Theory Comput.* **15**, 1896-1904 (2019).

57. J. Rodríguez-Carvajal, Recent advances in magnetic structure determination by neutron powder diffraction. *Phys. B: Condens. Matter* **192**, 55-69 (1993).

58. M. S. Modeling, Materials Studio, version 5.5, http://accelrys.com/products/collaborative-science/biovia-materials-studio.

59. A. Rogalev, F. Wilhelm, Magnetic circular dichroism in the hard X-ray range. *Phys. Met. Metallogr.* **116**, 1285-1336 (2015).

60. A. Rogalev, V. Gotte, J. Goulon, C. Gauthier, J. Chavanne, P. Elleaume, XAFS and X-MCD spectroscopies with undulator gap scan. *J. Synchrotron Rad.* **5**, 989-991 (1998).

61. K. V. Klementiev, VIPER for Windows. Freeware: http:\\www.desy.de/~klmn/viper.html.

62. E. B. Wilson, The normal modes and frequencies of vibration of the regular plane hexagon model of the benzene molecule. *Phys Rev.* **45**, 706-714 (1934).

63. S. Breda, I. D. Reva, L. Lapinski, M. J. Nowak, R. Fausto, Infrared spectra pyrazine, pyrimidine and pyridazine in solid argon. *J. Mol. Struct.* **786**, 193-206 (2006).

64. K. V. Berezin, V. V. Nechaev, P. M. Él'kin, Anharmonic resonances in the vibrational spectra of pyrazine. *J. Appl. Spectrosc.* **72**, 9-19 (2005).

65. J. F. Arenas, M. S. Woolley, I. L. Tocón, J. C. Otero, J. I. Marcos, Complete analysis of the surface-enhanced Raman scattering of pyrazine on the silver electrode on the basis of a resonant charge transfer mechanism involving three states. *J. Chem. Phys.* **112**, 7669-7683 (2000).

66. A. C. González-Baró, R. Pis-Diez, O. E. Piro, B. S. Parajón-Costa, Crystal structures, theoretical calculations, spectroscopic and electrochemical properties of Cr(III) complexes with dipicolinic acid and 1,10-phenantroline, *Polyhedron* **27**, 502-512 (2008).

67. B. Cadioli, E. Gallinella, C. Coulombeau, H. Jobic, G. Berthier, Geometric structure and vibrational spectrum of tetrahydrofuran. *J. Phys. Chem.* **97**, 7844-7856 (1993).

68. H. F. Shurvell, M. C. Southby, Infrared and Raman spectra of tetrahydrofuran hydroperoxide. *Vib. Spectrosc.* **15**, 137-146 (1997).

69. F. Cardarelli, Magnetic Materials. In *Materials Handbook: A Concise Desktop Reference* (Springer-Verlag, London Ltd, ed. 2, 2008), pp. 510-517.

70. M. S. Walmer, C. H. Chen, M. H. Walmer, A New Class of Sm-TM Magnets for Operating Temperatures Up to 550°C. *IEEE Trans. Magn.* **36**, 3376-3381 (2000)

71. R. Kütterer, H.- R. Hilzinger, H. Kronmüller, The temperature dependence of the coercive field of Co_5Sm magnets. *J. Magn. Magn. Mater.* **4**, 1-7 (1977).

72. J. C. Téllez-Blanco, X. C. Kou, R. Grössinger, E. Estévez-Rams, J. Fidler, B M. Ma, Coercivity and magnetic anisotropy of sintered Sm_2Co_{17}-type permanent magnets. *J. App. Phys.* **82**, 3928-3933 (1997).

73. C. Benabderrahmane, N. Béchu, P. Berteaud, M. E. Couprie, J. M. Filhol, C. Herbeaux, C. Kitegi, J. L. Marlats, K. Tavakoli, A. Mary, *Proceedings of the 11th European Particle Accelerator Conference*, Genoa, Italy, 23-27 June 2008, 2225-2227 (2008).

74. K. I. Pokhodnya, A. J. Epstein, J. S. Miller, Thin-Film $V[TCNE]_x$ Magnets. *Adv. Mater.* **12**, 410-413 (2000).

75. S. M. Holmes, G. S. Girolami, Sol-Gel Synthesis of $KV^{II}[Cr^{III}(CN)_6]\cdot 2H_2O$: A Crystalline Molecule-Based Magnet with a Magnetic Ordering Temperature above 100°C. *J. Am. Chem. Soc.* **121**, 5593-5594 (1999).

consent to its publication; **Competing interests:** the authors declare no competing interests; **Data and materials availability:** Crystallographic data of $Li_{0.7}[Cr(pyrazine)_2]Cl_{0.7} \cdot 0.25(THF)$ (**2•0.25(THF)**) at 290 and 500 K are available free of charge from the Cambridge Crystallographic Data Centre under reference numbers 1983877 and 2007863, respectively. All data are available in the main text or the supplementary materials.

Supplementary Materials:

Materials and Methods

Figures S1-S39

Tables S1-S10

References (*43-75*)

Science

AAAS

Supplementary Materials for

**Molecule-based metal-organic magnets with
large room-temperature coercivity and critical temperature up to 242°C**

Panagiota Perlepe, Itziar Oyarzabal*, Aaron Mailman, Morgane Yquel, Mikhail Platunov,
Iurii Dovgaliuk, Mathieu Rouzières, Philippe Negrier, Denise Mondieig, Elizaveta A. Suturina,
Marie-Anne Dourges, Sebastien Bonhommeau, Rebecca A. Musgrave, Kasper S. Pedersen,
Dmitry Chernyshov, Fabrice Wilhelm, Andrei Rogalev, Corine Mathonière
and Rodolphe Clérac*

*Correspondence to: itziar.oyarzabal@crpp.cnrs.fr (I. O.); clerac@crpp-bordeaux.cnrs.fr (R.C.)

This PDF file includes:

Materials and Methods
Figs. S1 to S39
Tables S1 to S10
References

Materials and Methods

All chemicals (lithium, 1,2-dihydroacenaphtylene 99% - CAS: 83-32-9, $CrCl_2$ 99.99%, pyrazine $\geq$ 99%) were purchased from commercial sources and used without further purification. $CrCl_2(pyz)_2$ and $Cr(OSO_2CH_3)_2(pyz)_2$ were synthesized as previously described (*26,27*). All manipulations were carried out in an Innovative Technology PureLab HE or an Mbraun Unilab glovebox under a dinitrogen or argon atmosphere and/or by standard Schlenk techniques. Tetrahydrofuran (THF) was dried with an Innovative Technology solvent-purification system and subsequently stored over 4 Å molecular sieves (H_2O content < 2 ppm, measured by a Metrohm 899 coulometer entry-level titrator). All reactions were carried out by using Pyrex glass-coated magnetic stirring bars and the resulting solid was manipulated with polypropylene or pyrex spatulas to avoid the presence of any magnetic impurity. Due to the extreme air and moisture sensitivity of the reduced compounds, all manipulations were performed under dinitrogen or argon atmosphere. To avoid the loss of intercalated THF molecules over time, the samples were stored inside the glovebox freezer at $T = 248$ K when not in use.

Synthesis of compound **1**: chemical reduction of $Cr(OSO_2CH_3)_2(pyz)_2$

$$Cr(OSO_2CH_3)_2(pyz)_2 \ + \ 2 \ Li^+[C_{12}H_{10}^{\bullet-}] \ \xrightarrow[-2 \ [C_{12}H_{10}]]{THF} \ \mathbf{1} \supset (Li_x(SO_3CH_3)_x) + (2-x) \ Li[SO_3CH_3]$$
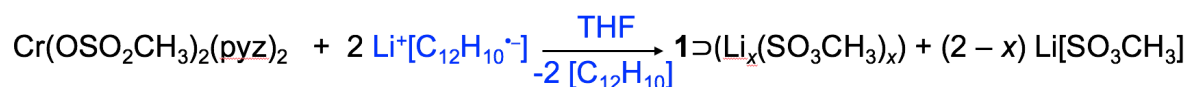
Lithium 1,2-dihydroacenaphtylenide was prepared by stirring 231.3 mg (1.5 mmol) of 1,2-dihydroacenaphtylene over a 10-fold excess of lithium metal (104 mg) in 8 mL of THF for 3 hours. The resulting dark olive (dark yellow-green) colored solution was filtered using a 0.2 μm PTFE membrane syringe filter and added dropwise to a stirred suspension of $Cr(OSO_2CH_3)_2(pyz)_2$ (286 mg, 0.71 mmol) in 5 mL of THF. The mixture was stirred for 4 days at room temperature and the resulting dark grey fine microcrystalline powder was separated by centrifugation, washed with THF, and allowed to stand in a nitrogen atmosphere for 10 minutes (see notes a) and b) below). Collected: 344 mg of solid.

Synthesis of $Li_{0.7}[Cr(pyz)_2]Cl_{0.7}\cdot(THF)$ (**2·(THF)**)

$$CrCl_2(pyz)_2 + 2 \ Li^+[C_{12}H_{10}^{\bullet-}] \ \xrightarrow[\substack{-1.3 \ LiCl \\ -2 \ [C_{12}H_{10}]}]{THF} \ \mathbf{2}\cdot\mathbf{(THF)} \ \xrightarrow{> 400 \ K} \ \mathbf{2}\cdot\mathbf{0.25(THF)}$$
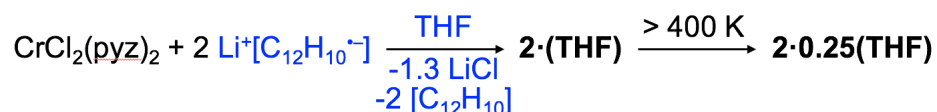
Chemical reduction of $CrCl_2(pyz)_2$ was accomplished following the same procedure as given for **1**, using $CrCl_2(pyz)_2$ (200 mg, 0.71 mmol) as precursor instead of $Cr(OSO_2CH_3)_2(pyz)_2$. The compound was filtered on a fine sintered glass Buchner funnel, washed with 2 ×15 mL of dry THF and dried for a few minutes under static vacuum (10^{-1} bar) at room temperature to afford a dark

brown solid (see notes c) to f) below). Yield of **2·(THF)**: ~200 mg, ~90 % yield based on $CrCl_2(pyz)_2$.

Comments on the synthesis:
a) $Cr(OSO_2CH_3)_2(pyz)_2$, product **1** and $Li[SO_3CH_3]$ are all insoluble in THF.
b) The color of product **1** (dark grey) contrasts notably with that of $Cr(OSO_2CH_3)_2(pyz)_2$ (light brown) suggesting the occurrence of a chemical modification during the course of the reaction. It is worth mentioning that $Li[SO_3CH_3]$ is a colorless solid and therefore its identification by PXRD led to the conclusion that the dark grey product **1** is a mixture of compounds.
c) The duration of the reaction (4 days) is crucial for the isolation of the phase-pure compound. The use of fewer than two equivalents of the reducing agent ($Li[C_{12}H_{10}]$) or shorter reaction times lead to a mixture of **2·(THF)** and $CrCl_2(pyz)_2$ phases, as determined by magnetic measurements.
d) The amount of THF in the final material decreases over time when **1** and **2·(THF)** are allowed to stand at room temperature and/or upon grinding, as evidenced by a mass loss and further demonstrated by FTIR measurements for **2·(THF)** (Fig. S22). Thus, the samples are habitually stored in a freezer (248 K) inside the glovebox to avoid the loss of intercalated solvent molecules that was confirmed by the constant weight of the samples over several months.
e) ICP measurements (*vide infra*) showed that under the employed synthetic conditions (amount of solvent and reaction time), the Cr:Li ratio in the final compound was of 1:0.7(1) (based on nine different batches). The Cr:Cl ratio of ca. 1:0.7 was independently estimated from the XANES data at the Cl *K*-edge (Fig. S11). The Cr:Li and Cr:Cl ratios were further confirmed by EA (Table S6) and gravimetric analysis of the LiCl that remained in solution after the reaction. For such purpose, the THF fractions were combined and the volatiles flash distilled to afford a beige solid. The organic residues were extracted with toluene and the insoluble solid, assumed to be LiCl, was collected on a pre-weighted, fine sintered glass funnel. The mass of the solid obtained by difference, 0.0374 g, was consistent with the presence of 1.3 LiCl equivalents (expected value: 0.0391 g) in the filtrate.
f) The "drying" of **2·(THF)** was performed by heating the solvate in a capped but only partially sealed screw cap-vial at 400 K for 18 hours or at 500 K for 10 hours under dinitrogen or argon atmosphere. However, ~25 % of the THF remained in the final material, leading to the general formulation $Li_{0.7}[Cr(pyz)_2]Cl_{0.7}·0.25(THF)$, **2·0.25(THF)** (Table S6). Further drying of the material under dynamic vacuum (> 10^{-2} bar) was unsuccessful as **2·0.25(THF)** readily decomposed, as verified by both the FTIR (Fig. S24) and EA measurements.

Elemental analyses
Samples for C, H, N were prepared in pre-weighed $6 \times 6 \times 10$ mm Sn foil pans, typically using 3-5 mg of solid sample. The pans were transferred to the analyzer sealed in 0.5 mL Eppendorf Flex-tube® microcentrifuge tube and placed inside a separate vial under Argon. The pre-calibrated Vario EL III element analyzer was used to determine the C, H, N weight percentage from sample masses (obtained by weighing by difference the pre-weighted centrifuge tube and Sn foil pan

before quickly transferring them to the sampling chamber). The error on the C, H and N values is estimated between 0.5% and 0.1 % (0.1 % corresponds to the error in the ideal standard conditions given by Vario). The results are summarized in Table S6.

Inductively coupled plasma (ICP) – optical emission spectroscopy (OES)
ICP-OES measurements were performed on two different spectrometers, which required different sample preparations:
(a) Samples were prepared by refluxing approximately 10 mg of solid in a mixture of 1 mL of HNO_3 (65 %) and 1 mL of HCl (37 %) under argon atmosphere and diluting to 100 mL with Milli-Q water. Samples were analyzed by ICP-OES on a Varian ICP/OES 720 ES spectrometer.
(b) Samples were prepared by digesting approximately 20 mg of solid in 10 mL of hot concentrated HNO_3 (65 %) in a sealed pressure vessel under argon and diluting to 20 mL with Milli-Q water. Samples were analyzed by ICP-OES on a Perkin-Elmer Optima 4300 DV ICP optical emission spectrometer for simultaneous multi-element detection.
Measurements carried out on nine independently prepared samples of **2·(THF)** gave an average Cr:Li ratio of 1:0.7 with an estimated standard deviation of 0.1 (the experimental values are 1:0.65, 0.67, 0.52, 0.77, 0.64, 0.85, 0.73, 0.69, 0.71).

Fourier-transform infrared spectroscopy
FTIR spectra of neat, solid samples were recorded on a Bruker Alpha Platinum single reflection diamond ATR module using 24 scans at 4 cm^{-1} resolution in an argon filled glovebox. For convenience, the spectra are plotted as the transmittance versus the wavenumber ($T = 10^{-A}$ with A being the absorbance).

Raman spectroscopy
Raman scattering measurements were carried out in backscattering geometry using a commercial (XploRA, Horiba scientific) confocal Raman spectrometer equipped with a motorized xy stage, a 1200 grooves/mm grating, and a long working distance ×50 Olympus objective with 0.45 numerical aperture. The samples were loaded into quartz capillaries of 0.5 mm diameter and irradiated at 785 nm with an 0.37 mW laser power. The integration time was 3 minutes and two accumulations were performed.

Computational details
Molecular model calculations on the X-ray structure fragments were done with ORCA 4.1 (*43*,*44*) package. The positions of the hydrogen atoms were added and optimized using the B3LYP (*45*,*46*,*47*,*48*) method and def2-TZVP (*49*) basis set. The exchange interactions were calculated at the same level of theory using the broken-symmetry approach (Ising Hamiltonian) assuming that the exchange coupling between the Cr spin and each pyrazine radical spin is the same. The spin-Hamiltonian of the $[Cr(pyz)_4]^{4-}$ model complex can be written using an Ising model considering

Cr-radical interactions (J_{Cr-R}) and interactions between two radicals in *trans*-positions (J_{RR}) and in *cis*-positions ($J_{R'R}$):

$$H = -2J_{Cr-R} \sum_{i=1-4} S_z^{Cr} S_{z,i}^R - 2J_{RR} \sum_{\substack{i=1,2 \\ j=3,4}} S_{z,i}^R S_{z,j}^R - 2J_{R'R} \sum_{i=1,3} S_{z,i}^R S_{z,i+1}^R$$

The exchange parameters can be estimated using the energies of the broken-symmetry solutions (see Table S9):

$$J_{Cr-R} = -\frac{E_{aaaaA} - E_{bbbbA}}{16}$$

$$J_{RR} = -\frac{E_{aaaaA} + E_{bbbbA} - 2E_{ababA}}{8}$$

$$J_{R'R} = -\frac{E_{aaaaA} + E_{bbbbA} + 2E_{ababA} - 4E_{abbaA}}{8}$$

Geometry optimization and frequency calculations together with Raman intensities were calculated using Gaussian16 (*50*) for neutral and reduced pyrazine ligands and molecular fragments of the Cr complex using different methods and basis sets detailed below.

X-ray absorption spectra of Cl *K*-edge were simulated using orbital energies (*51*) calculated with the pure functional BP86 (*52,53*) and scalar relativistic approximation ZORA with relativistic version of def2-TZVP basis set (*54*) and CP(PPP) basis for Cr, while spin-orbit coupling (*55,56*) was accounted as a perturbation. The spectra were plotted using 0.7 eV line width (Fig. S12).

Thermogravimetric analysis - mass spectrometry (TGA-MS)
TGA-MS for compound **2·(THF)** was performed under argon on a NETZSCH STA 449 F5 Jupiter® coupled with QMS 403 D Aëolos Quadro (Erich NETZSCH GmbH & Co. Holding KG, Selb, Germany) thermogravimetric analyzer with a heating rate of 5 K min^{-1}. Due to the extreme air sensitivity of the compound, the pre-weighed sample (8.6 mg) was covered with anhydrous cyclohexane (14.13 mg) inside a N_2-filled glovebox. The pan containing the suspension was kept inside a closed vial and it was quickly transferred to the TGA-MS instrument after removing the vial from the glovebox.

Powder X-ray diffraction (PXRD)
Microcrystalline powder samples were loaded into 0.5 mm borosilicate glass capillaries inside a glovebox under a dinitrogen atmosphere, and the capillaries were sealed with wax. High-resolution powder X-ray diffraction data were subsequently collected at beamline BM01 (part of the Swiss-Norwegian Beamlines, SNBL) at the European Synchrotron Radiation Facility (ESRF) in Grenoble, France. Diffraction patterns were collected with a wavelength of 0.6673 and 0.7829 Å for compounds **1** and **2·(THF)**, respectively. For the variable-temperature PXRD studies, the

sample was heated under a dinitrogen stream using a Cryostream 700+ with a 6 K min^{-1} ramping rate.

The indexing of the powder X-ray diffraction patterns, Pawley refinements, structure solution, and the final Rietveld refinement were performed with the Fullprof (*57*) and Materials Studio (*58*) programs. The refinement of the crystal structure of **2·0.25(THF)** (Table S7) was performed on a powder pattern collected at 500 K (Fig. S27) and at 290 K after cooling from 500 K (Fig. 3). The refinement was done considering the size-strain anisotropic peak broadening of the powder patterns and preferred orientation along [100] direction (Modified March's function). Using CrCl$_2$(pyz)$_2$ (CCDC 1563526) as a structure model, the following atomic restrains for the pyrazine rings were used: $d_{(N-N)}$ = 2.90 Å, $d_{(N-C)}$ = 1.35 Å, $d_{(C-C)short}$ = 1.33 Å, $d_{(C-C)long}$ = 2.56 Å with σ = 0.001 Å and $d_{(C-C)}$ = 1.62 Å between disordered pyrazine rings with σ = 0.01 Å. Atomic displacement parameters were refined isotropically at first: independently for Cr, with the same B_{iso} for C, N and Cl, and with a 1.5B_{iso} of C, N and Cl for Li. Finally, they were fixed and the B(overall) was refined together with atomic coordinates. The Li/Cl content was fixed at 0.7 according to the ICP, EA, gravimetric (*vide supra*) and XANES data (Fig. S11). It is worth mentioning that THF molecules were not found and thus were not included in the final structural model.

X-ray absorption spectroscopy (XAS):

X-ray absorption experiments have been performed at the ID12 beamline (*59*) of the European Synchrotron Radiation Facility (ESRF). For the Cr *K*-edge experiments, the X-ray source was the first harmonic of APPLE-II type helical undulator (HU-38), whereas for the Cl *K*-edge ones, it was the first harmonic of HELIOS-II-type helical undulator (HU-52) in pure helical mode. The advantage of using helical mode is that the content of the higher order harmonics is strongly reduced, since only the fundamental harmonic is emitted on the undulator axis. The X-ray beam was monochromatized using a fixed-exit double-crystal monochromator equipped with a pair of Si(111) crystals. Powdered samples mixed with mineral oil were mounted inside argon filled glove-box into vacuum tight sample holders covered with 13-μm thick kapton foil. X-ray absorption near edge structure (XANES) spectra were recorded using total fluorescence yield detection mode. The X-ray fluorescence signal from the samples were collected in the back-scattering geometry, through the kapton window, using Si photodiodes. The Cr *K*-edge extended X-ray absorption fine structure (EXAFS) spectra were measured in transmission mode using an optimized "gap-scanning technique" (*60*). The processing of experimental EXAFS spectra was done using the Viper software (*61*). No corrections for the phase and amplitude of backscattering atoms were applied. Local magnetic properties of the Cr site at 295 K were studied using X-ray magnetic circular dichroism (XMCD) method at the Cr *K*-edge. The XMCD spectra were obtained as the difference between two consecutive XANES spectra recorded with opposite photon helicities of the incoming photons under external magnetic field produced by a superconducting solenoid. Measurements were performed for both directions of applied magnetic field parallel and antiparallel to the incoming X-ray wavevector in order to ensure the absence of experimental

artifacts. The element-selective magnetization curve was recorded by monitoring the maximum of XMCD signal as a function of an applied magnetic field.

Magnetic measurements

The characterization of the magnetic properties was performed on a Quantum Design SQUID magnetometer MPMS-XL operating between 1.8 and 400 K for applied *dc* fields ranging from –7 to 7 T. The measurements were performed on microcrystalline samples (~10 mg) sealed in polyethylene bag (size ~ 3 × 0.5 × 0.02 cm), which was subsequently sealed into a polypropylene bag to allow measurements up to 400 K. The additional polypropylene bag was also used to protect the samples, which are extremely sensitive to air and moisture. The magnetic data were corrected for the *in-situ* sample decomposition above 300 K, the intrinsic diamagnetic contributions of the sample and sample holder. The magnetic data for **1** (Figs. S2-S4) were calculated based on the molecular weight of the $Cr(OSO_2CH_3)_2(pyz)$ precursor (402.39 g mol^{-1}).

The high-temperature magnetic characterization (up to 540 K) was performed on a Microsense Vibrating Sample Magnetometer (VSM) for applied *dc* fields ranging from –1.8 to 1.8 T. The microcrystalline powder (~10 mg) was loaded into a quartz tube of ~4 mm internal diameter and sealed with epoxy glue to second quartz tube of ~4 mm external diameter. The preparation of the sample was carried in a glovebox under inert atmosphere (Ar or N_2). The zero field-cooled (ZFC)/field-cooled (FC) magnetization data were collected on samples of **2·(THF)** (Fig. 4) and **2·0.25(THF)** (Fig. S35) introduced first in the magnetometer at 300 K under zero field. Magnetization data were obtained while warming in the presence of a magnetic field of 50 Oe (ZFC) and subsequently cooling (FC) to room temperature under the same magnetic field. The high-temperature VSM *M* vs. *H* data (400-520 K) were scaled to the results obtained at 300 and 400 K from the SQUID MPMS magnetometer.

Electrical conductivity

Resistivity measurements on **1**, **2·(THF)** and **2·0.25(THF)** were carried out using a home-made 4-point probe installed inside a Quantum Design PPMS-9 system working between 1.8 and 400 K. Acquisitions were performed with the use of an external device (Keithley 2401 source-meter). These measurements were performed on pellets of polycrystalline samples (typically 7 mm diameter and 1 mm thickness; about 50-60 mg) prepared under dinitrogen atmosphere with a manual press. The pellets were loaded in the homemade resistivity cell allowing the four aligned needle probes (mounted on springs) to be in contact with the pellet.

Table S1.
Summary of the magnetic properties of selected chromium powder, nanoparticles and oxides. AF = antiferromagnet; F = ferromagnet; T_N = Néel temperature; T_C = Critical or Curie temperature.

Sample (size/shape)	Magnetic property	Reference
Cr bulk	AF, T_N = 311 K	(*32*)
Cr powder/strained	AF, T_N = 450-475 K	(*33,34*)
Cr nanoparticles (2 nm)	Curie paramagnetism	(*35*)
Cr nanoparticles (13-73 nm)	Their magnetic properties are extremely sensitive to surface oxide layers. Paramagnetism or AF ($T_N \leq$ 310 K) or F order can be observed.	(*36*)
$Cr^{III}_2O_3$ bulk	AF, T_N = 308 K	(*37*)
$Cr^{IV}O_2$ bulk	F, T_C = 392(6) K	(*38*)
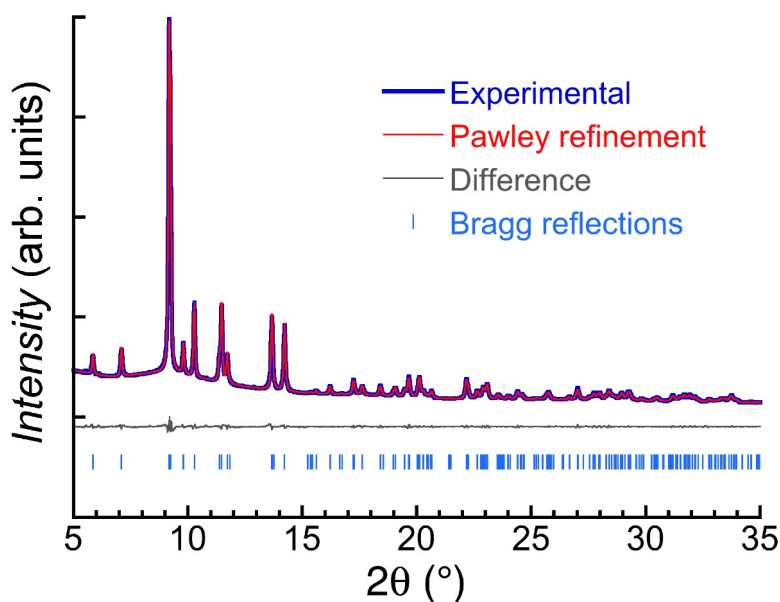
Fig. S1.
Synchrotron X-ray powder diffraction pattern of **1** (solid blue line), collected at room-temperature (298 K) with a wavelength of 0.6673 Å and its Pawley refinement (solid red line). The Pawley refinement led to *C2/m* space group with $a = 7.8081(5)$ Å, $b = 7.4473(5)$ Å, $c = 6.5356(4)$ Å and $\beta = 90.561(3)°$, similar to what found for $Li[CH_3SO_3]$ ($a = 7.8586(16)$ Å, $b = 7.4889(15)$ Å, $c = 6.5454(13)$ Å and $\beta = 90.234(15)°$, *29*). The difference (solid gray line) between the best Pawley fit (solid red line) and the experimental data (solid blue line), and calculated line positions (blue bars) are also shown in the figure. Considering that the Bragg diffraction peaks correspond exclusively to the salt $Li[CH_3SO_3]$, these data suggest that the Cr-based magnet present in **1**, is poorly crystalline, nanocrystalline or amorphous.
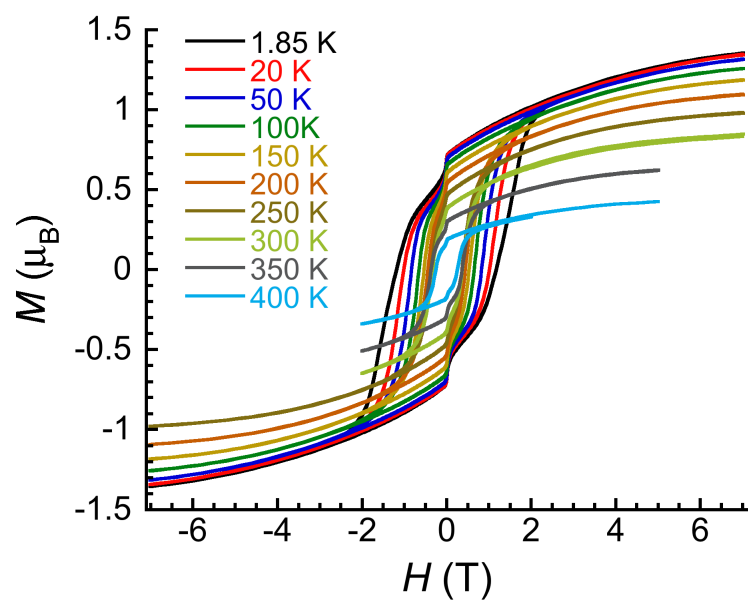
Fig. S2.

Magnetization versus applied *dc* magnetic field data (at 7 to 8 Oe s^{-1}) in the -7 to 7 T field range for **1** at selected temperatures from 1.85 K and increasing the temperature up to 400 K. As the exact composition of **1** is unknown, the magnetization data were normalized using the molecular weight of the $Cr(OSO_2CH_3)_2(pyz)_2$ parent compound.
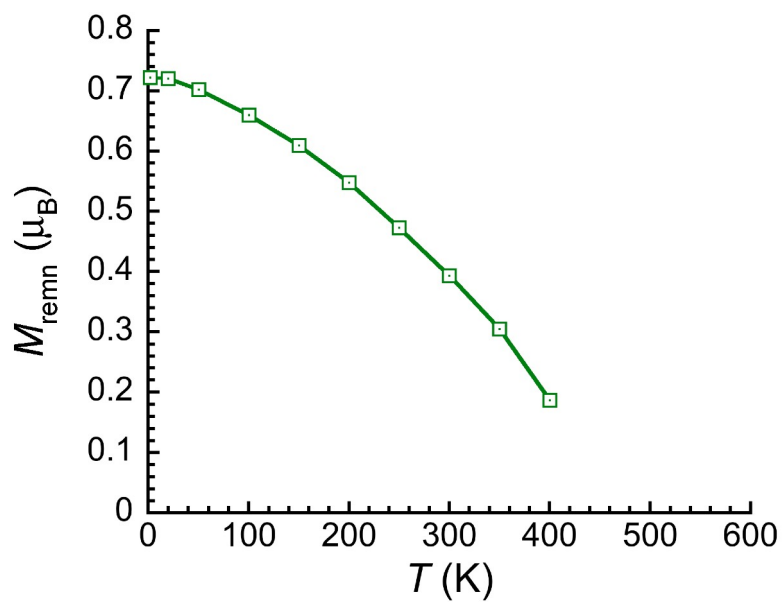
Fig. S3.

Temperature dependence of the remnant magnetization, M_{remn}, determined from the M vs. H data (Fig. S2) at each temperature for **1**. As the exact composition of **1** is unknown, the magnetization data were normalized using the molecular weight of the $Cr(OSO_2CH_3)_2(pyz)_2$ parent compound. The green line is a guide for the eye.
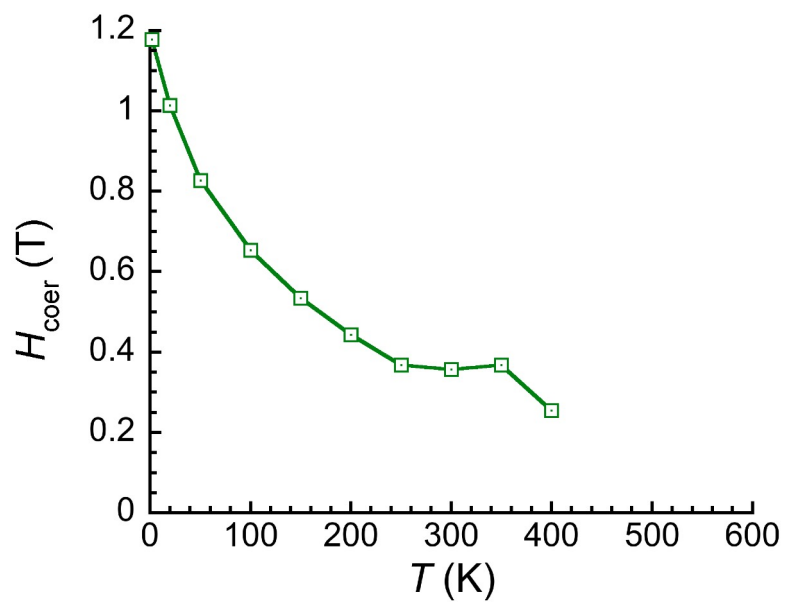
Fig. S4.

Temperature dependence of the coercive field, H_{coer}, determined from the M vs. H data (Fig. S2) at each temperature for **1**. The green line is a guide for the eye.
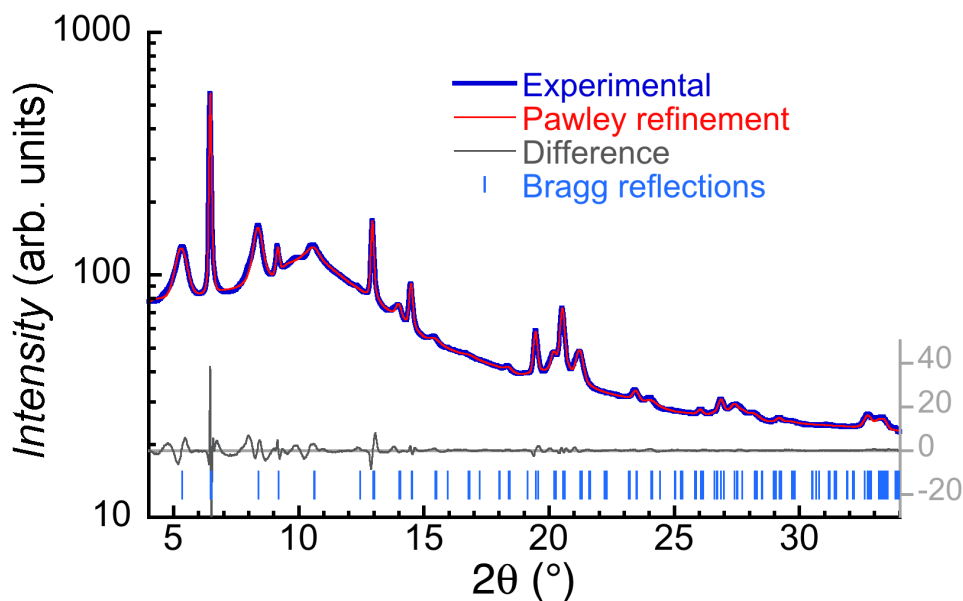
Fig. S5.

Synchrotron X-ray powder diffraction pattern of **2·(THF)** (solid blue line), collected at room-temperature (298 K) with a wavelength of 0.7829 Å and its Pawley refinement (solid red line; R_p = 1.33 % and R_{wp} = 1.75 %). The Pawley refinement led to an orthorhombic *Pmmm* space group with the following cell parameters: a = 6.9239(9) Å, b = 6.9524(2) Å and c = 8.478(2) Å. The difference (solid gray line) between the best Pawley fit (solid red line) and the experimental data (solid blue line), and calculated line positions (blue bars) are also shown in the figure.
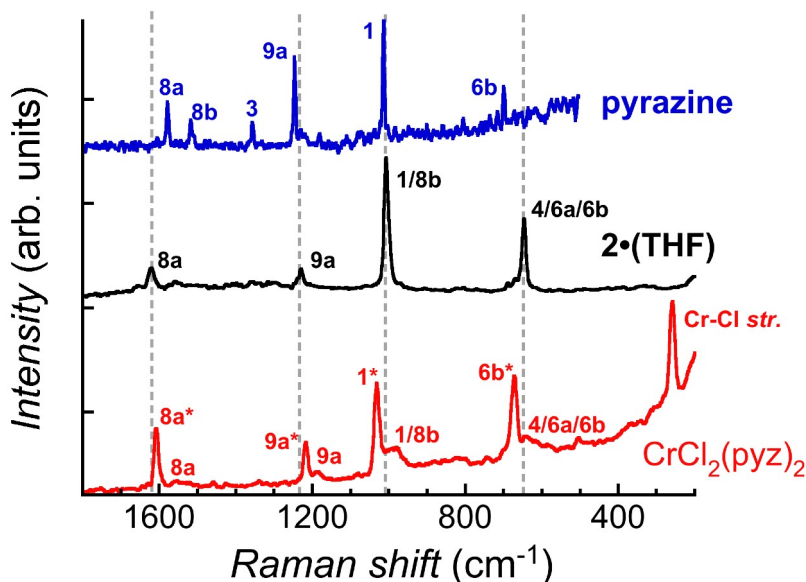
Fig. S6.

Normalized Raman spectrum (λ = 785 nm) of neutral pyrazine (pyz; blue trace), **2·(THF)** (black trace) and $Cr^{III}Cl_2(pyz)_2$ (red trace) between 1800 and 200 cm^{-1} recorded at room temperature. The labelling denotes the Wilson nomenclature (*62*; * denotes neutral pyrazine ligands). Peak assignment of pyrazine[†]: 1578 cm^{-1} – **8a**; 1518 cm^{-1} – **8b**; 1356 cm^{-1} – **3**; 1246 cm^{-1} – **9a**; 1013 cm^{-1} – **1**; 700 cm^{-1} – **6b**. Tentative peak assignment of **2·(THF)**[†,‡]: 1620 cm^{-1} – **8a**; 1229 cm^{-1} – **9a**; 1007 cm^{-1} – **1** and/or **8b**; 646 cm^{-1} – **4**, **6a** or **6b**. The spectra of **2·(THF)** does not show any bands corresponding to THF, which could be due to partial evaporation of THF before (grinding of the samples to load them into quartz capillaries) and/or during the measurements (heat generated during the irradiation of the sample). Tentative peak assignment of $Cr^{III}Cl_2(pyz)_2$[†,‡,§]: 1607 cm^{-1} – **8a***; ~ 1556 cm^{-1} – **8a**; 1218 cm^{-1} – **9a***; ~1187 cm^{-1} – **9a**; 1031 cm^{-1} – **1***; ~ 979 cm^{-1} – **1** and/or **8b**; 673 cm^{-1} – **6b***; ~ 638 cm^{-1} – **4**, **6a** or **6b**; 260 cm^{-1} – *sym* Cr-Cl stretching.

[†] **8a**: *sym.* C=C stretching; **8b**: a*sym.* C-N stretching; **3**: C-H rocking; **9a**: C-H scissoring; **1**: C-H scissoring, in-plane ring-breathing; **6b**: *asym.* in-plane ring-deformation; **4**: C-H twisting, *asym.* out-of-plane ring-deformation; **6a**: *sym.* in-plane ring-deformation. These assignments are consistent with those proposed in the literature for IR spectra of pyrazine (*63*).
[‡] Detailed computational analysis of optimized geometries, vibrational frequencies and Raman activities of neutral and reduced pyrazine are shown in Table S2. The chosen method, PBE0/def2-QZVP level, reproduces the experimental structure of neutral pyrazine with 0.01 Å accuracy (Table S3) and the harmonic frequencies together with the Raman activities, which agree with previous theoretical studies (*64*). There is little information available for the Raman spectra of reduced pyrazine, however, Raman surface scattering at silver electrodes indicated that the reduction of pyrazine leads to low energy shift of all observed bands (*65*). Thus, in the experimental spectra of the parent compound, $Cr^{III}Cl_2(pyz)_2$, the most intense peaks are assigned
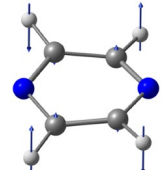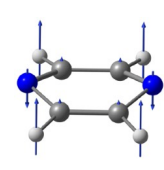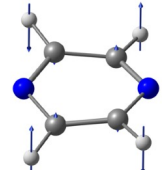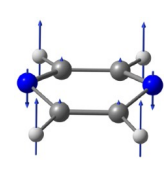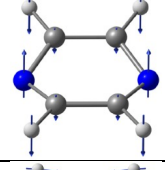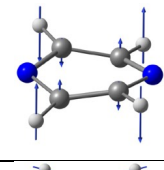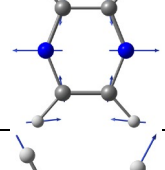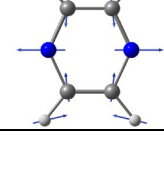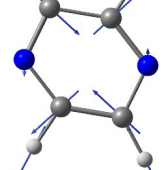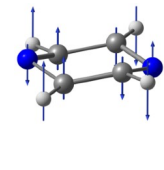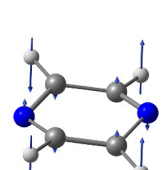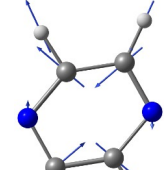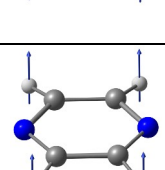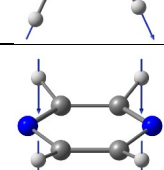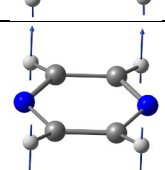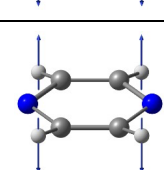
to neutral pyrazine (denoted with *), while the shoulders can tentatively be assigned to the reduced pyrazine in this mixed valence compound. In contrast, the well-defined peaks in **2·(THF)** strongly suggest the presence of only reduced pyrazine, as expected for complete reduction of all pyrazine ligands.
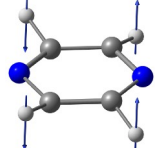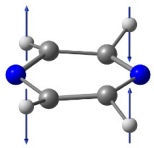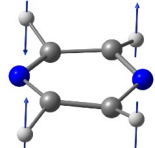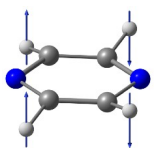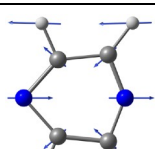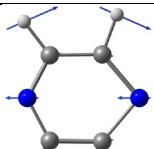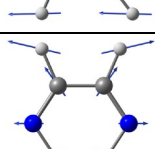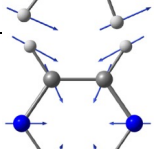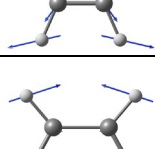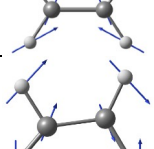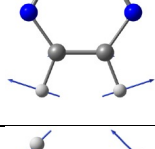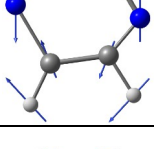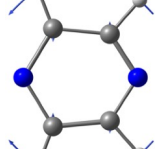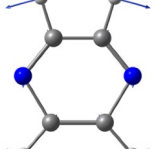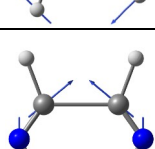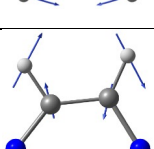
The calculated vibrational frequency analysis given in Table S2 shows that the highest intensity peak at 1059 cm^{-1} (**1**, according to Wilson notation) is associated with the C-H scissoring and ring breathing mode and predicted to shift to lower frequency by 54 cm^{-1} upon reduction. However, the band **8b** that corresponds to *asym*. C-N stretching shifts by ~ 600 cm^{-1} and almost overlaps with **1** when pyrazine is reduced. Moreover, **4** shifts by ~100 cm^{-1} and gains significant intensity upon reduction. This computational analysis reflects the difficulty in assigning the experimental spectra of reduced pyrazine, which has been attributed to both the shift in the fundamental frequencies and to the changes in Raman activities of certain bands (*65*).
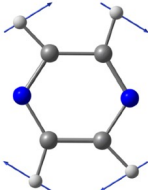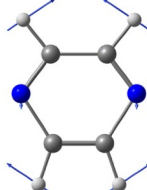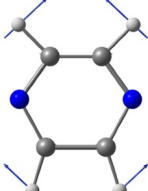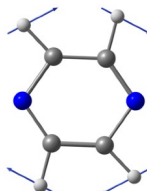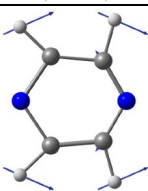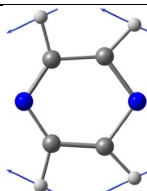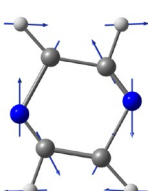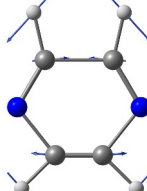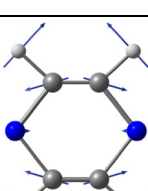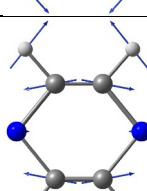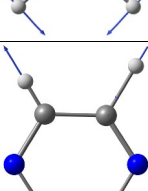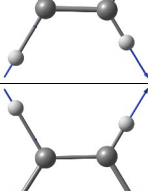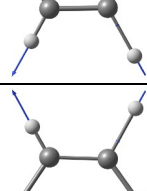
§ The band at 260 cm^{-1} in the $Cr^{III}Cl_2(pyz)_2$ parent compound can be assigned to the symmetric Cr-Cl stretching (*66*), as supported by harmonic frequency calculations of the gas phase optimized structure of $[CrCl_2(pyz)_4]^\circ$ (B3LYP/def2-SVP, calculated value = 263 cm^{-1}).

Table S2.

Normal mode analysis and Raman activities computed for neutral and reduced pyrazine at PBE0/def2-QZVP level. The most active Raman bands observed in our experimental window (Fig. S6) are highlighted by a blue background.

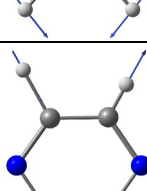| #	Neutral pyrazine					Reduced pyrazine				
	Wilson notation	Symmetry		$\bar{\nu}$, cm^{-1}	Raman Activity	Wilson notation	Symmetry		$\bar{\nu}$, cm^{-1}	Raman Activity
1	16a	A$_u$		350	0	16b	B$_{3u}$		269	0
2	16b	B$_{3u}$		433	0	16a	A$_u$		418	0
3	6a	A$_g$		607	2	**6a**	A$_g$		578	7
4	**6b**	B$_{3g}$		721	6	**4**	B$_{2g}$		682	5
5	4	B$_{2g}$		788	1	**6b**	B$_{3g}$		711	5
6	11	B$_{3u}$		810	0	11	B$_{3u}$		733	0
7	10a	B$_{1g}$		954	0	10a	B$_{1g}$		803	0

8	5	B_{2g}		1004	0	17a	A_u		823	0
9	17a	A_u		1018	0	5	B_{2g}		874	4
10	12	B_{1u}		1039	0	12	B_{1u}		981	0
11	1	A_g		1059	50	1	A_g		1005	37
12	15	B_{2u}		1099	0	8b	B_{3g}		1039	25
13	18a	B_{1u}		1177	0	15	B_{2u}		1068	0
14	14	B_{2u}		1255	0	18a	B_{1u}		1084	0
15	9a	A_g		1259	16	9a	A_g		1232	17

16	3	B₃g		1375	1	19b	B₂u		1302	0
17	19b	B₂u		1451	0	3	B₃g		1365	7
18	19a	B₁u		1528	0	19a	B₁u		1453	0
19	8b	B₃g		1617	6	14	B₂u		1475	0
20	8a	Ag		1643	21	8a	Ag		1637	117
21	7b	B₃g		3166	134	7b	B₃g		3080	202
22	13	B₁u		3167	0	13	B₁u		3082	0
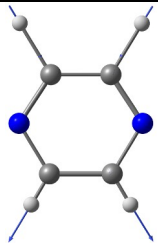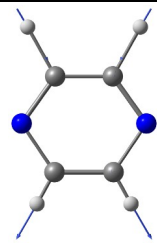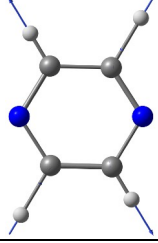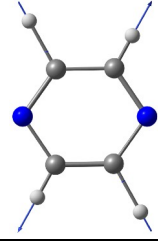
| 23 | 20b | B$_{2u}$ | | 3181 | 0 | 20b | B$_{2u}$ | | 3108 | 0 |
| 24 | 2 | A$_g$ | | 3187 | 380 | 2 | A$_g$ | | 3115 | 510 |

Table S3.

Computed harmonic frequencies ($\bar{\nu}$, in cm^{-1}) and Raman activities of neutral and reduced pyrazine using PBE0 with different basis sets. It is worth noting that the relative intensities of Raman spectra are strongly basis set dependent. Nevertheless, Def2-QZVP is the largest basis set that should thus be considered as the best choice to describe experimental results. The red boxes without background indicated the regions of the experimental Raman spectra where bands are observed in Fig. S6.

| def2-QZVP				def2-TZVP				def2-SVP				aug-cc-pVDZ				6-31++G**			
neutral		reduced		neutral		reduced		neutral		reduced		neutral		reduced		neutral		reduced	
$\bar{\nu}$	Activity	$\bar{\nu}$	Activity	$\bar{\nu}$	Activity	$\bar{\nu}$	Activity	$\bar{\nu}$	Activity	$\bar{\nu}$	Activity	$\bar{\nu}$	Activity	$\bar{\nu}$	Activity	$\bar{\nu}$	Activity	$\bar{\nu}$	Activity
350	0	269	0	350	0	280	0	351	0	296	0	349	0	226	1	348	0	230	0
433	0	418	0	433	0	421	0	441	0	419	0	430	0	423	0	431	0	407	0
607	2	578	7	607	3	578	4	603	3	577	4	604	2	574	1122	605	3	575	425
721	6	682	5	721	6	678	2	727	7	672	3	717	5	675	1	721	7	664	0
788	1	711	5	788	0	711	6	791	1	720	6	779	0	706	9	775	1	711	10
810	0	733	0	809	0	731	0	810	0	746	0	805	0	729	0	807	0	732	0
954	0	803	0	955	0	813	1	953	2	832	10	947	0	819	40	949	0	819	109
1004	0	823	0	1000	0	857	0	1006	0	908	0	983	0	890	0	988	0	884	0
1018	0	874	4	1015	0	871	0	1017	0	918	0	1004	0	910	0	999	0	889	9
1039	0	981	0	1039	0	979	0	1036	0	983	12	1034	0	985	0	1036	0	986	0
1059	50	1005	37	1060	47	1006	40	1067	37	986	0	1057	56	1003	3554	1059	50	1004	1135
1099	0	1039	25	1099	0	1026	12	1101	0	1018	34	1097	0	1066	157	1102	0	1050	187
1177	0	1068	0	1178	0	1067	0	1178	0	1076	0	1172	0	1069	0	1179	0	1074	0
1255	0	1084	0	1259	16	1085	0	1253	21	1085	0	1253	17	1078	0	1264	17	1083	0
1259	16	1232	17	1259	0	1234	21	1305	0	1231	31	1279	0	1225	3044	1281	0	1238	1036
1375	1	1302	0	1374	1	1303	0	1363	1	1327	0	1362	1	1307	0	1375	2	1319	0
1451	0	1365	7	1451	0	1365	6	1456	0	1355	6	1444	0	1356	19	1454	0	1369	23
1528	0	1453	0	1527	0	1454	0	1528	0	1450	0	1518	0	1444	0	1529	0	1457	0
1617	6	1475	0	1618	6	1482	0	1649	7	1513	0	1623	7	1475	0	1628	7	1481	0
1643	21	1637	117	1645	19	1646	44	1663	18	1674	28	1651	23	1630	19450	1653	23	1633	8025
3166	134	3080	202	3168	137	3077	207	3180	149	3068	227	3183	135	3102	167	3197	142	3109	172
3167	0	3082	0	3169	0	3079	0	3181	0	3071	1	3184	0	3103	0	3198	0	3111	0
3181	0	3108	0	3184	0	3106	0	3194	0	3096	0	3199	0	3129	0	3212	0	3137	0
3187	380	3115	510	3190	371	3113	523	3201	383	3107	537	3204	389	3135	2296	3217	391	3143	1250
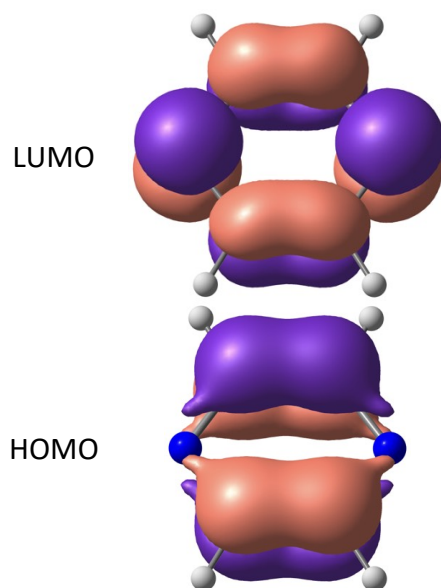
Fig. S7.

Highest occupied molecular orbital (HOMO) and lowest unoccupied molecular orbital (LUMO) of a neutral pyrazine molecule. The LUMO orbital features bonding C–C and antibonding C–N interactions, leading to shortening of the former and lengthening of the latter upon reduction (Table S4).

Table S4.

Bonds lengths (Å) for DFT-optimized structures of neutral and reduced pyrazines.

	Experiment	PBE0/def2-QZVP		PBE0/def2-TZVP		PBE0/def2-SVP		PBE0/aug-cc-pVDZ		PBE0/6-31++G**	
	neutral (*64*)	neutral	reduced	neutral	reduced	neutral	reduced	neutral	reduced	neutral	reduced
N−C	1.3376(13)	1.326	1.369	1.327	1.370	1.329	1.372	1.333	1.373	1.333	1.373
C−C	1.3968(37)	1.388	1.368	1.389	1.368	1.397	1.376	1.396	1.378	1.395	1.377
C−H	1.0831(37)	1.085	1.090	1.086	1.092	1.096	1.103	1.092	1.097	1.088	1.093

Table S5.

Gas phase optimized (B3LYP/def2-TZVP) molecular fragments of $[CrCl_2(pyz)_4]^{-q}$, $[CrCl(pyz)_4]^{1-q}$, $[Cr(pyz)_4]^{2-q}$ where $q = 0, 1, 2, 3$ and 4. The highest point group symmetry (with $R < 0.01$) and Mulliken spin population on the Cr site (in parentheses) are shown above each structure (Mulliken spin population values close to 3 and 4 correspond to Cr^{III} and Cr^{II}, respectively). The bond lengths in the first coordination sphere are shown in Å.

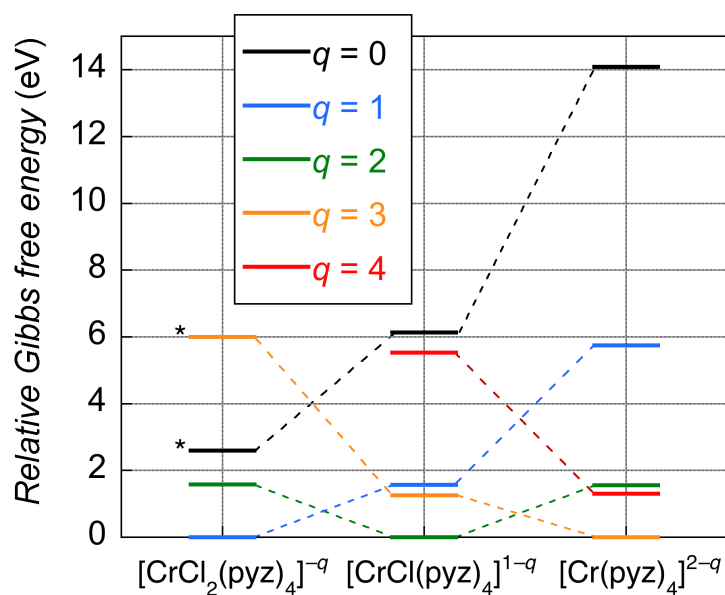| q	$[CrCl_2(pyz)_4]^{-q}$	$[CrCl(pyz)_4]^{1-q}$	$[Cr(pyz)_4]^{2-q}$
0	D_4 (3.2)	C_4 (4.0)	D_4 (4.2)
1	D_2 (4.1)	C_2 (4.0)	C_1 (4.7)
2	C_2 (4.1)	C_1 (4.0)	D_2 (4.3)
3	D_4 (3.2)	C_4 (4.1)	D_2 (4.2)
4	Both Cl⁻ dissociate, no minimum found	C_2 (4.1)	D_4 (4.2)

Fig. S8.

Calculated gas phase (B3LYP/def2-TZVP) relative Gibbs free energy (in eV) of molecular fragments of $[CrCl_2(pyz)_4]^{-q}$, $[CrCl(pyz)_4]^{1-q}$ and $[Cr(pyz)_4]^{2-q}$ where q = 0, 1, 2, 3 and 4 is the number of added electrons. The * symbols indicate the states with a Cr^{III} metal ion, while others possess a Cr^{II} center as illustrated by the fragment structures given in Table S5. These calculations establish that reduction of the pyrazine ligands is more favorable and facilitated by the complete dissociation of the chloride ligands, as indicated by the relative stability of $[Cr(pyz)_4]^{2-q}$ where q = 3 or 4, compared to $[CrCl(pyz)_4]^{1-q}$ and $[CrCl_2(pyz)_4]^{-q}$ derivatives.
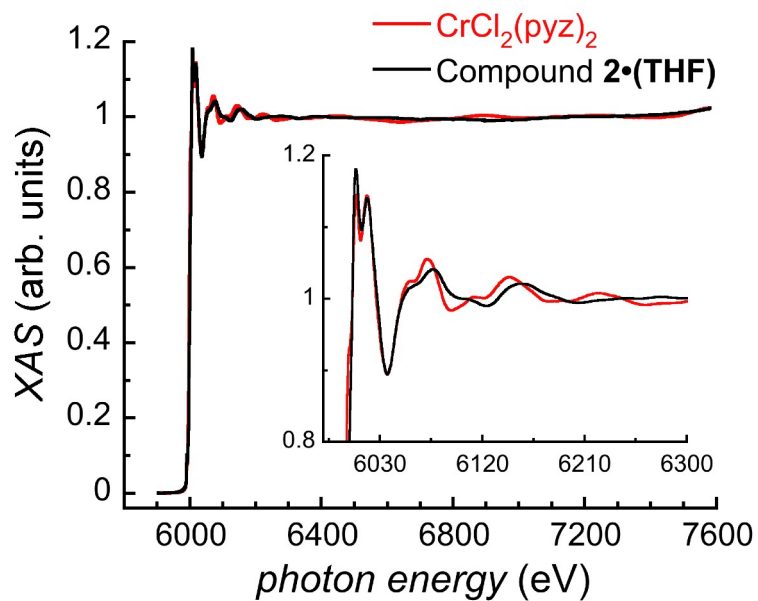
Fig. S9.

Normalized XAS spectra at the Cr *K*-edge for **2·(THF)** (black line) and CrCl₂(pyz)₂ (red line), at 295 K. Inset: magnified view of the spectra in the EXAFS region.
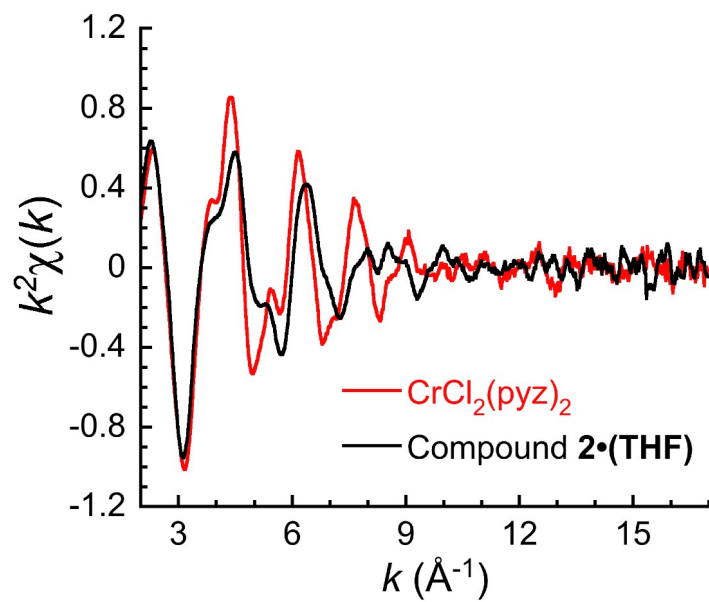
Fig. S10.

k^2-weighted EXAFS spectra at the Cr K-edge for compound **2·(THF)** (black line) and $CrCl_2(pyz)_2$ (red line) at 295 K.

Table S6.
Elemental analysis results for **2·(THF)** and **2·0.25(THF)**.[*]

	C (%)	H (%)	N (%)
2·(THF) Sample 1 - 1st measurement	46.53	5.127	18.01
2·(THF) Sample 1 - 2nd measurement	44.47	5.137	17.82
2·(THF) Sample 1 - 3rd measurement	45.61	5.164	18.19
2·(THF) Sample 2	44.79	4.683	17.34
2·(THF) Sample 3 - 1st measurement	46.65	5.195	17.56
2·(THF) Sample 3 - 2nd measurement	45.55	5.023	17.88
Average (ESD) for 2·(THF)	**45.60(88)**	**5.05(19)**	**17.80(31)**
Calc. for $Li_{0.7}[Cr(pyz)_2]Cl_{0.7}$·(THF)	**45.91**	**5.14**	**17.84**
After heating at 400 K the compound **2·(THF)** (average on 6 measurements with ESD)	41.71(53)	3.84(37)	21.81(121)
After heating at 480-500 K the compound **2·(THF)** (average on 6 measurements with ESD)	41.13(96)	3.66(19)	21.82(106)
Calc. for $Li_{0.7}[Cr(pyz)_2]Cl_{0.7}$·0.25(THF)	**41.60**	**3.88**	**21.56**

[*] The CHN-analysis were performed without the addition of a V_2O_5 additive (to avoid additional weighing errors) and the variation of the C percentages could be caused by the formation of metal carbide during the combustion cycle.
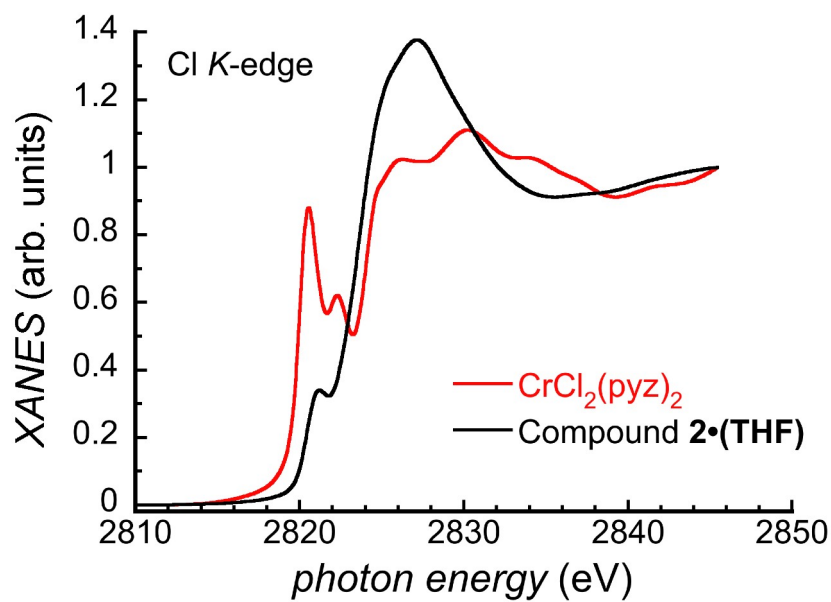
Fig. S11.
Normalized XANES spectra at the Cl *K*-edge of **2·(THF)**[*] (black line) and CrCl₂(pyz)₂ (red line) recorded at 295 K.

[*]Considering the raw XANES spectra at the Cl *K*-edge of **2·(THF)** and CrCl₂(pyz)₂ measured in the exact same experimental conditions (including the same sample holder) with only a few minutes of intervals, it is possible to evaluate at about 0.74, the respective amount of chloride per chromium in **2·(THF)** knowing that two chlorides are present in CrCl₂(pyz)₂ (see below the calculations for two sets of measurements on two different **2·(THF)** samples).

First set of measurements:

Compounds	Intensity at 2810.7 eV	Intensity at 2845.8 eV	Difference	Average	Cl amount in 2·(THF)
CrCl₂(pyz)₂	0.3614	2.6256	2.2642	2.2664	
CrCl₂(pyz)₂	0.3507	2.6194	2.2687		
2·(THF) sample 1	0.4191	1.2427	0.8236	0.8482	0.75 per Cr
2·(THF) sample 1	0.3666	1.2394	0.8728		

Second set of measurements:

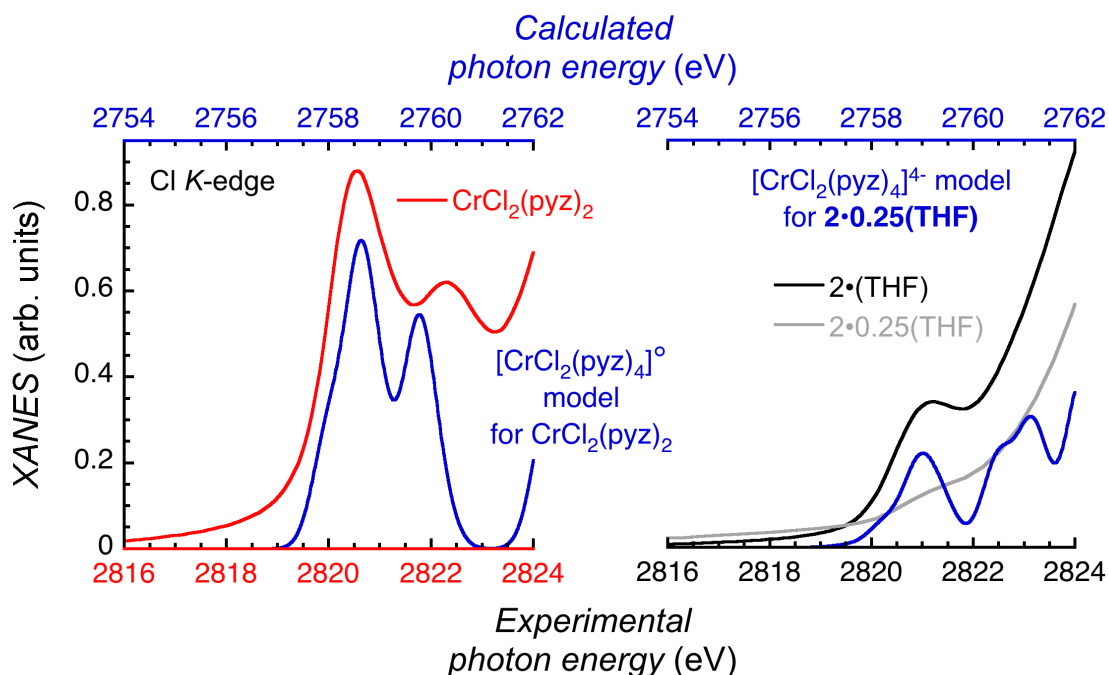| Compounds	Intensity at 2810.7 eV	Intensity at 2845.8 eV	Difference	Average	Cl amount in 2·(THF)
CrCl₂(pyz)₂	0.2181	1.9202	1.7021	1.7036	
CrCl₂(pyz)₂	0.2169	1.9220	1.7051		
2·(THF) sample 2	0.2450	0.8698	0.6248	0.6245	0.73 per Cr
2·(THF) sample 2	0.2447	0.8689	0.6242		

Fig. S12.

Calculated (BP86/def2-TZVP/ZORA, linewidth of 0.7 eV) XANES spectra at the Cl K-edge (excitations from Cl 1s orbital) of the molecular fragments (i) $[CrCl_2(pyz)_4]^{4-}$ taken from structural model of **2·0.25(THF)** (Fig. 3; $d_{Cr\cdots Cl} = 3.598$ Å, blue trace on the right plot) and (ii) $[CrCl_2(pyz)_4]°$ taken from X-ray structure of $CrCl_2(pyz)_2$ ($d_{Cr\text{-}Cl} = 2.337$ Å, blue trace on the left plot, *26*). For comparison, the pre- and rising Cl K-edge regions of the normalized experimental XANES spectra for **2·(THF)** (black trace), for **2·0.25(THF)** (grey trace) and $CrCl_2(pyz)_2$ (red trace) are shown at 295 K. The calculated spectra (top x-axis; blue traces) are shifted by 62 eV from the experimental ones, but the energy shift and loss of intensity associated with Cl dissociation and change of Cr oxidation state are well reproduced.
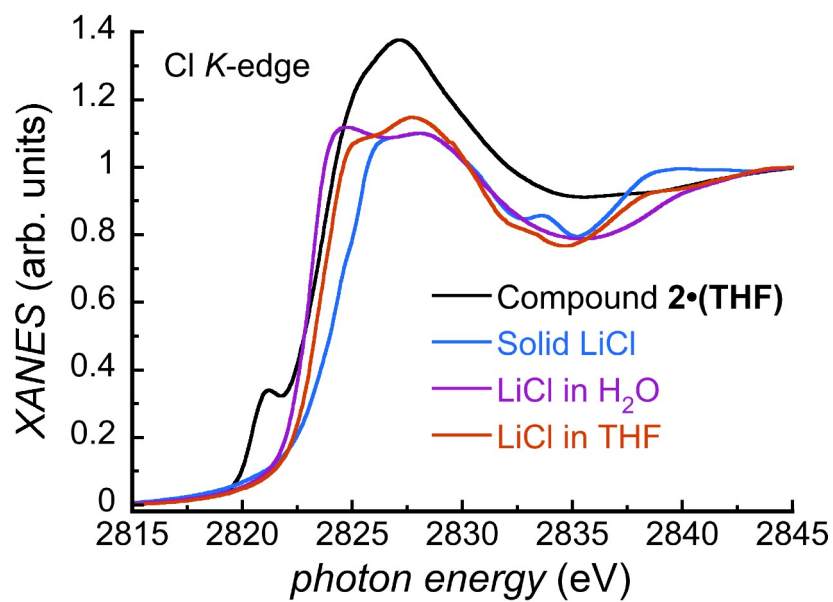
Fig. S13.

Normalized XANES spectra at the Cl *K*-edge of **2·(THF)** (black line) and LiCl in its solid form (blue line) and in aqueous (purple line) and THF (red line) solutions recorded at 295 K. It is worth noting that LiCl XANES spectra in both solution and solid state do not display any near-edge feature. These results are in contrast with the observation of a detectable near-edge signal in **2·(THF)** indicating that chlorides are still in enough electronic proximity to the Cr^{II} ions in the structure.
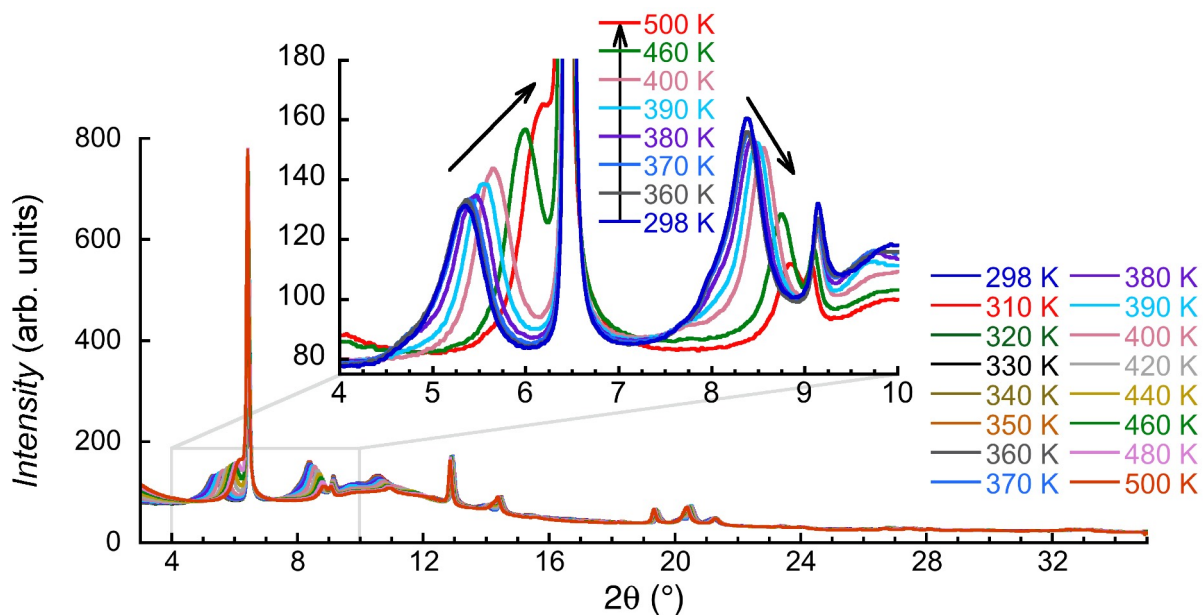
Fig. S14.

Temperature dependence of the synchrotron powder X-ray diffraction patterns of **2·(THF)**, collected between 298 and 500 K with a heating rate of 6 K min^{-1} ($\lambda = 0.7829$ Å). Inset: magnified view of the low-angle region (4-10°) for selected temperatures highlighting the diffraction shifts at the structural change above 380 K linked to the THF partial loss (see main text).
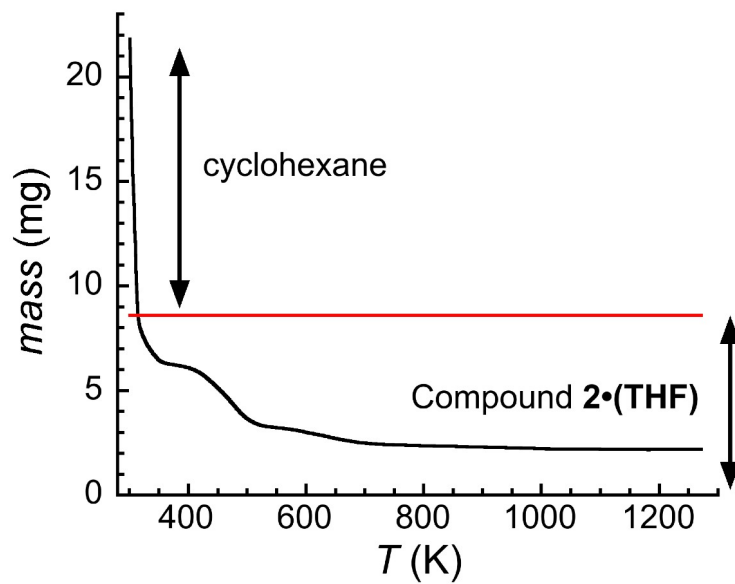
Fig. S15.

Thermogravimetric analysis (TGA) of **2·(THF)** under a flow of argon at a 5-K min^{-1} heating rate. The initial mass drop corresponds to cyclohexane (14.13 mg) that was used to protect the sample (8.6 mg). Note that even though the initial mass was of 22.73 mg, 0.946 mg of cyclohexane evaporated during the furnace closing and temperature stabilization. Therefore, the initial mass in the TGA spectra is of 21.784 mg, which was obtained at 301.15 K.
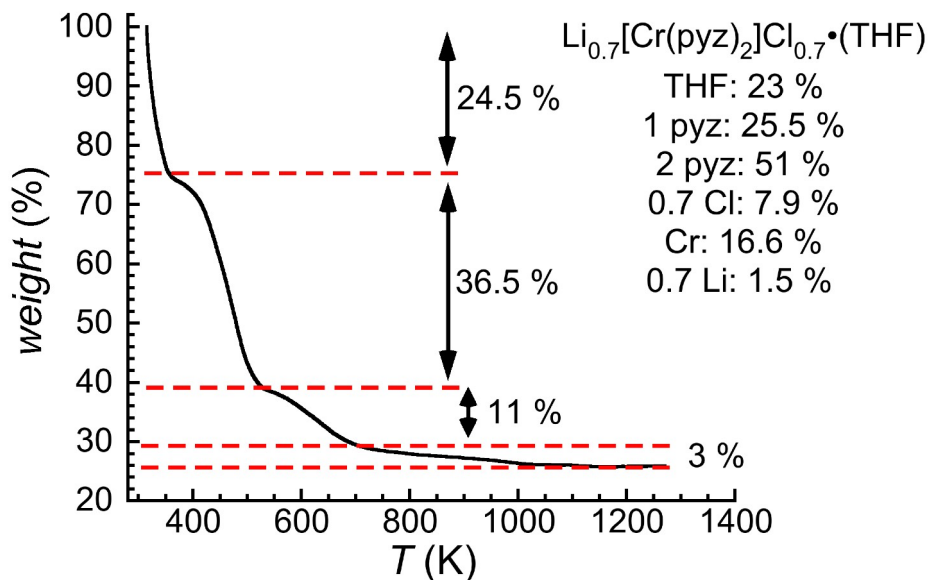
Fig. S16.

Thermogravimetric analysis (TGA) of **2·(THF)** derived from Fig. S15 after removing the mass corresponding to cyclohexane (at 5 K min^{-1}). Expected weight percentages for Li$_{0.7}$[Cr(pyz)$_2$]Cl$_{0.7}$·(THF): 1 THF, 23.0 %; 1 pyz, 25.5 %; 2 pyz, 51 %; 0.7 Cl, 7.9 %; Cr, 16.6 %; 0.7 Li, 1.5 %. Thermogravimetric analysis - mass spectrometry (TGA-MS) measurements (Fig. S17-S20) indicate that (a) the 1st step between 300-355 K (24.5 %) corresponds to the loss of almost one THF, (b) the 2nd (355-520 K, 36.5 %) and the 3rd (520-700 K, 11 %) steps originate the loss of pyrazine ligands and/or decomposition products of pyrazine, in addition to some residual THF that was not evaporated in the 1st step, (c) the 4th (above ~700 K, 3 %) step is due to a partial loss of chloride. The residual weight percentage (25 %) agrees with the sum expected for lithium, chromium, and the remaining chloride amount (23 %). The premature decomposition of the compound below 520 K can be ascribed to the way of preparing and heating the sample in the TGA experiment, as the material is clearly stable at least up to 520 K when heated in closed containers (under argon or dinitrogen), as confirmed by powder X-ray diffraction (Fig. S14) and magnetic (Fig. 4) measurements.
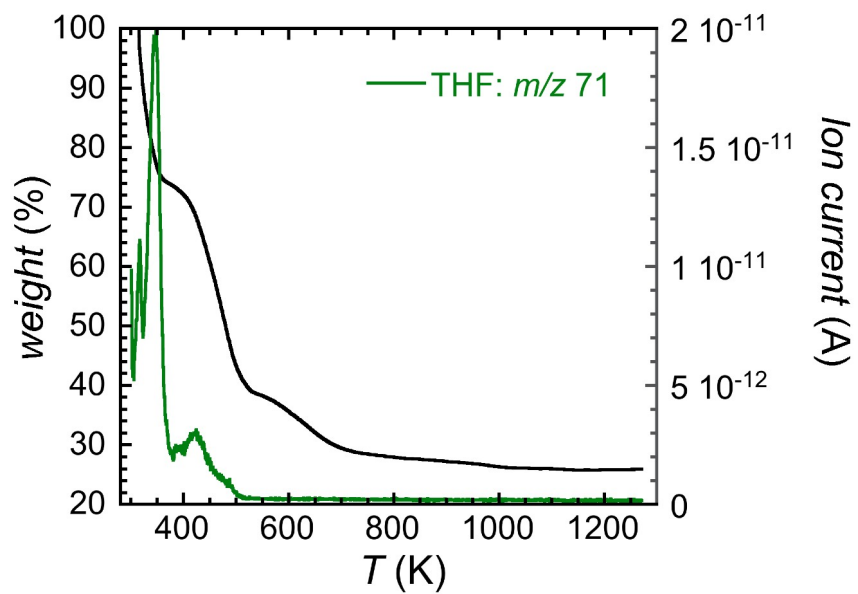
Fig. S17.

TGA-MS thermogram showing the weight loss in **2·(THF)** (black line; at 5 K min^{-1}) highlighting the THF loss and the corresponding ion current at $m/z = 71$ ($C_4H_7O^+$ fragment, green line).
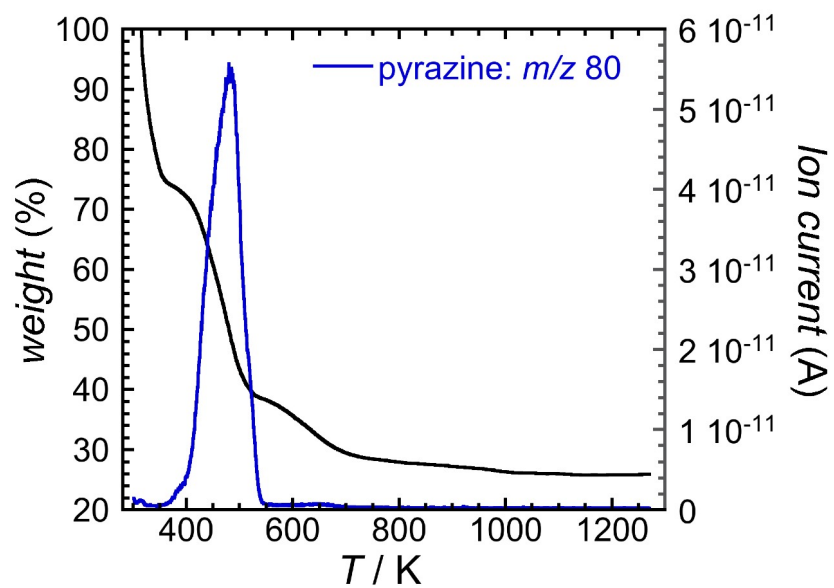
Fig. S18.

TGA-MS thermogram showing the weight loss in **2·(THF)** (black line; at 5 K min^{-1}) highlighting the pyrazine loss and the corresponding ion current at $m/z = 80$ (blue line).
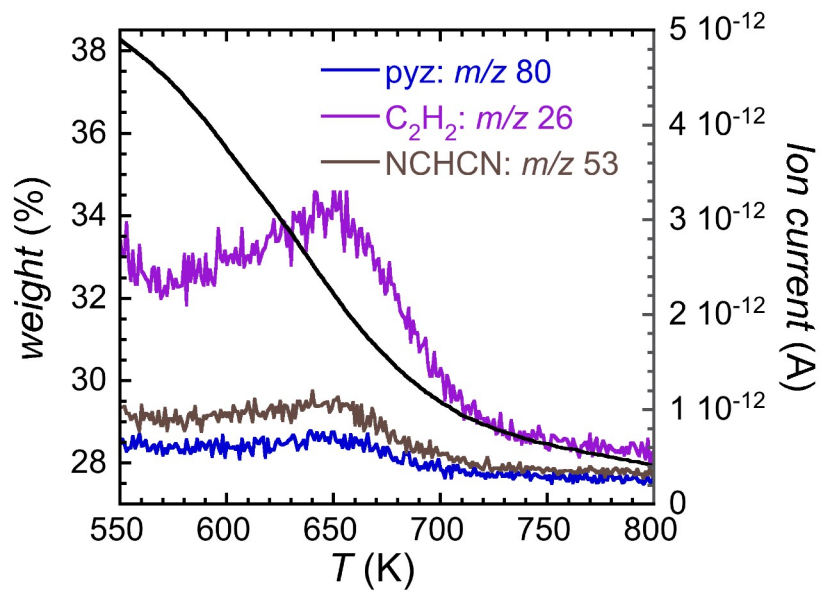
Fig. S19.

Magnified view of the TGA-MS thermogram showing the weight loss in **2·(THF)** (black line; at 5 K min^{-1}) highlighting the loss of pyrazine (ion current at $m/z = 80$, blue line) and decomposition products of pyrazine (ion current at $m/z = 26$, C_2H_2, purple line; ion current at $m/z = 53$, NCHCN, brown line).
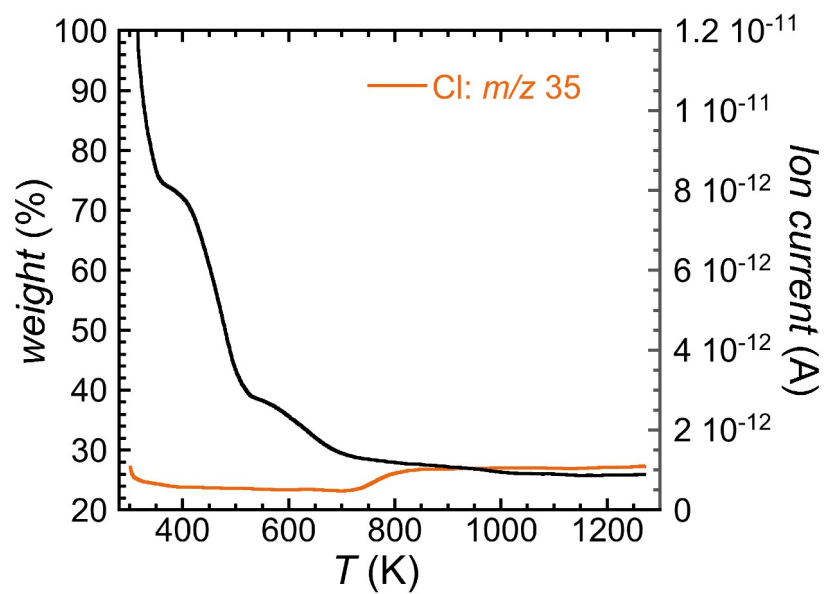
Fig. S20.

TGA-MS thermogram showing the weight loss in **2·(THF)** (black line; at 5 K min^{-1}) highlighting the chlorine loss and the corresponding ion current at *m/z* = 35 (orange line).
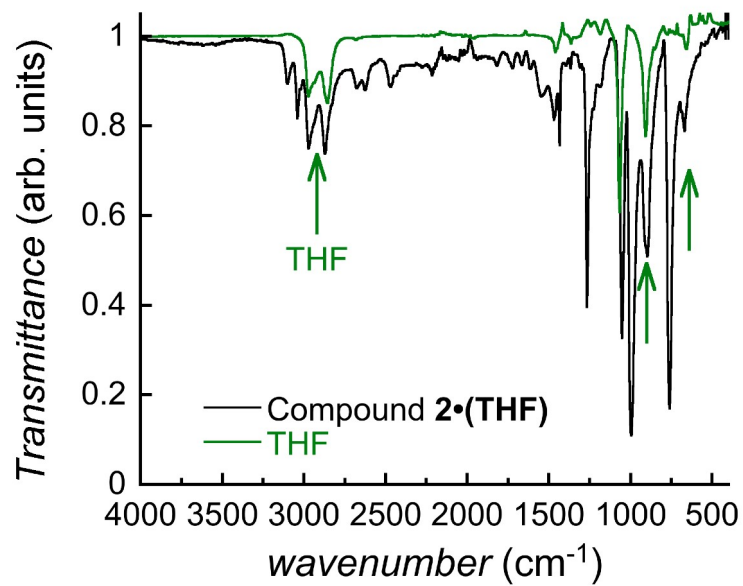
Fig. S21.

ATR-FTIR spectra collected at room temperature for **2·(THF)** (black line) and THF (green line). Peak assignment for the most intense bands of THF (*67,68*): 2972 cm^{-1}, asymmetric C–H stretching; 2856 cm^{-1}, symmetric C–H stretching; 1066 cm^{-1}, ring stretching; 906 cm^{-1}, ring breathing; 657 cm^{-1}, CH$_2$ wagging. The green arrows (↑) denote the areas in which the most relevant THF bands are observed in **2·(THF)** (note that the band at 1066 cm^{-1} of THF overlaps with pyrazine bands).
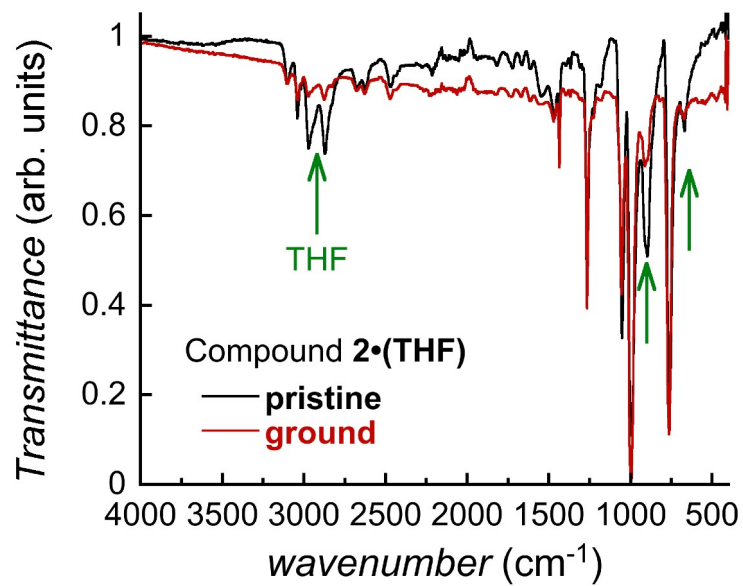
Fig. S22.

ATR-FTIR spectra collected at room temperature for **2·(THF)** (black line) and a ground sample (red line). The green arrows (↑) denote the areas in which the main differences between pristine and ground **2·(THF)** are observed, which agree well with the areas in which the most intense bands of THF appear (note that the band at 1066 cm^{-1} of THF overlaps with pyrazine bands).
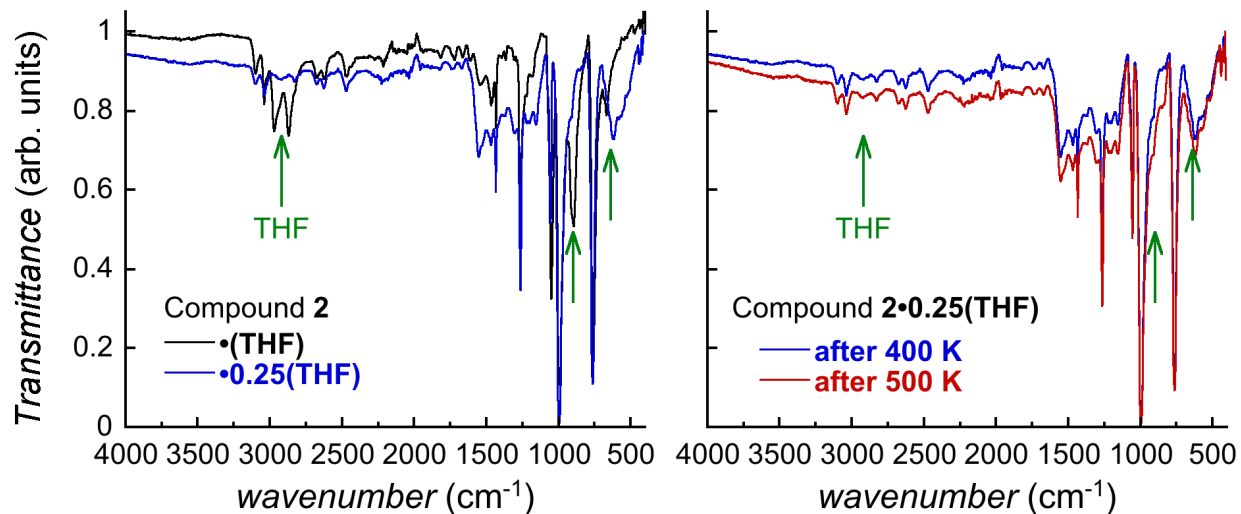
Fig. S23.
ATR-FTIR spectra collected at room temperature for **2·(THF)** (black line) and **2·0.25(THF)** after a 400-K treatment (18 hours; blue lines) and after a 500-K treatment (10 hours; red line). Left: green arrows (↑) denote the areas in which the main differences between **2·(THF)** and **2·0.25(THF)** are observed, which agree well with the areas in which the most intense bands of THF appear (note that the band at 1066 cm^{-1} of THF overlaps with pyrazine bands). Right: green arrows (↑) denote the areas in which the most intense bands of THF should appear (note that the band at 1066 cm^{-1} of THF overlaps with pyrazine bands).
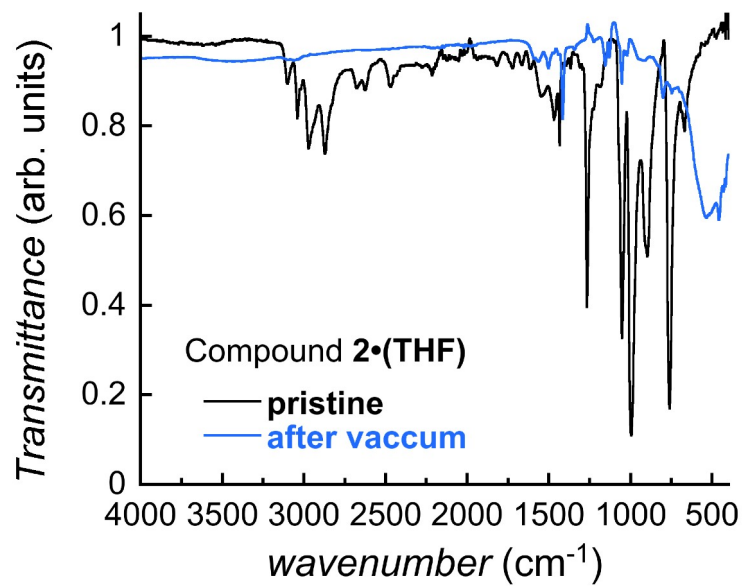
Fig. S24.

ATR-FTIR spectra collected at room temperature for **2·(THF)** (black line) and a sample exposed to dynamic vacuum (10^{-3} bar, blue line). The significant differences between both spectra indicate the decomposition of the material.
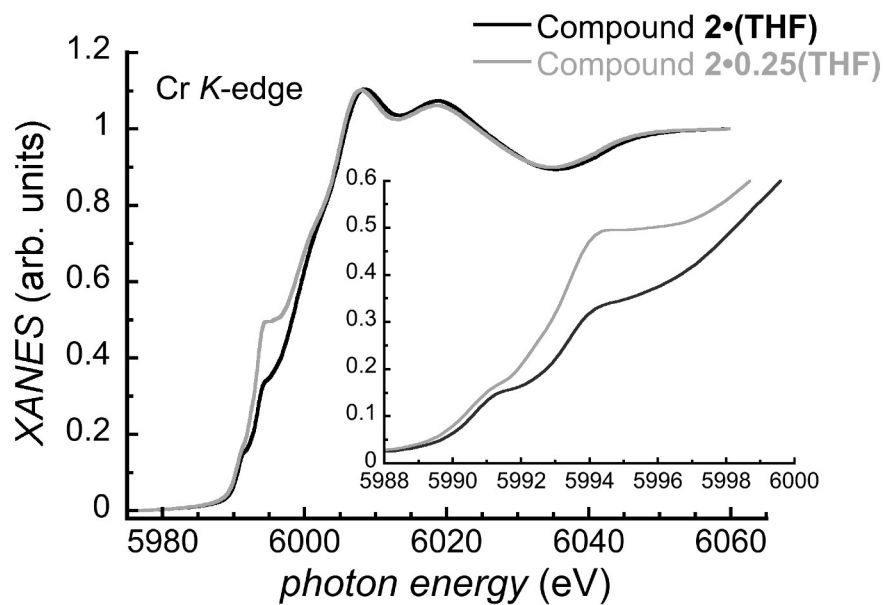
Fig. S25.

Normalized XANES spectra at the Cr *K*-edge of **2·(THF)** (black line) and **2·0.25(THF)** (grey line) recorded at 295 K. Inset: magnified view of the spectra in the near-edge region.
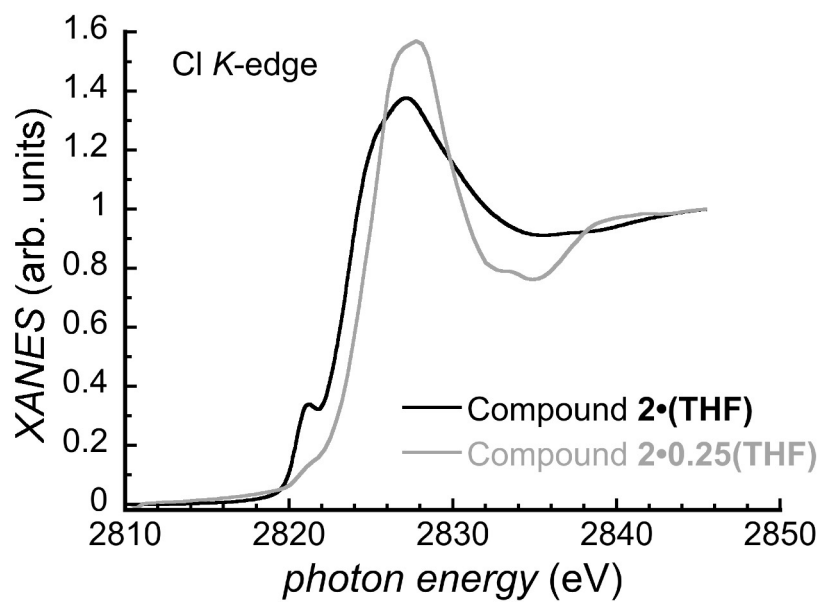
Fig. S26.

Normalized XANES spectra at the Cl *K*-edge of **2·(THF)** (black line) and **2·0.25(THF)** (grey line) recorded at 295 K.
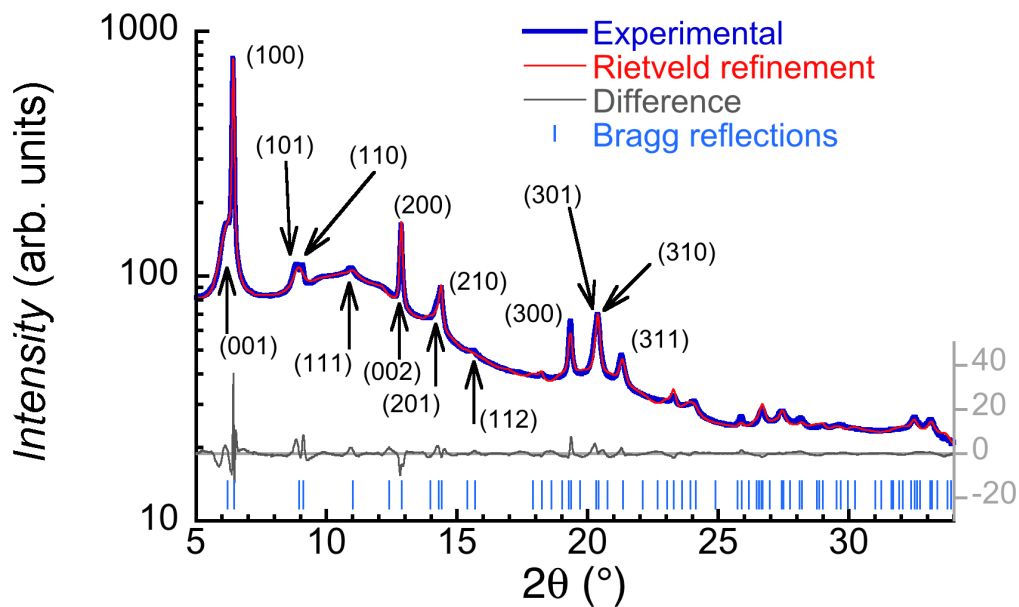
Fig. S27.

Synchrotron powder X-ray diffraction pattern of **2·0.25(THF)** collected at 500 K with a wavelength of 0.7829 Å. The best Rietveld refinement (red line; R_I = 3.14 %) of the synchrotron PXRD pattern of **2·0.25(THF)** at 500 K (blue line) is shown together with the experimental/model difference (grey line) and calculated line positions (blue bars). The resulting structural model is the same as the one shown in Figs. 3B-C. The indexation of the main diffraction peaks is shown.

Table S7.

Crystallographic parameters of the structural model for **2·0.25(THF)** obtained from the best Rietveld refinement of the powder X-ray diffraction pattern collected at 500 K (Fig. S27) and at 290 K after cooling from 500 K (Fig. 3).

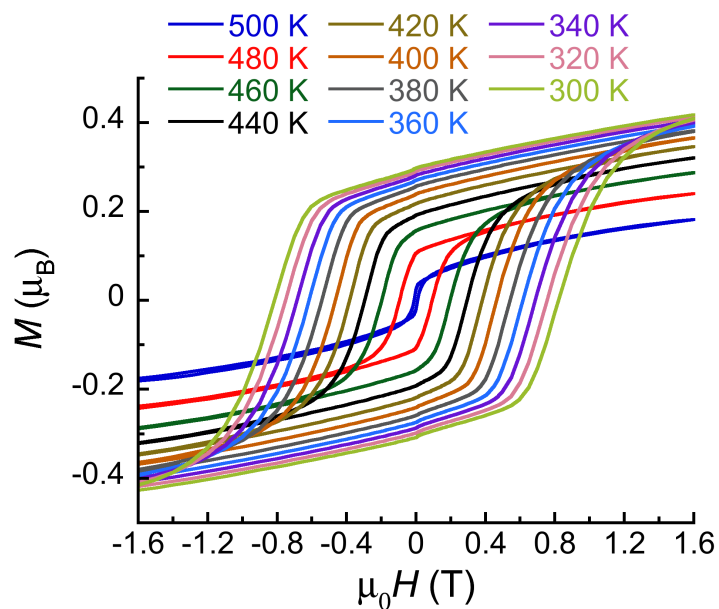| Temperature	500 K	290 K
CCDC number	2007863	1983877
Crystal system	tetragonal	tetragonal
Space group	$P4/mmm$	$P4/mmm$
a / Å	6.99618(13)	6.98932(14)
b / Å	6.99618(13)	6.98932(14)
c / Å	7.273(3)	7.195(3)
Volume / Å^3	355.97(14)	351.46(13)
Z	1	1
Observed reflections	96	93
Parameters	13	13
Restraints	5	5
GOF	4.11	4.54
R_p	1.559	1.632
R_{wp}	2.145	2.324

Fig. S28.

Magnetization versus applied *dc* magnetic field data (at 8 to 12 Oe s^{-1}) in the −1.6 to 1.6 T field range for **2·(THF)** (and thus for **2·0.25(THF)** after partial desolvation above 400 K). These data were collected after the *M* vs. *H* hysteresis plots shown in Figs. 4B-C, during the cooling process from 520 K to room temperature.
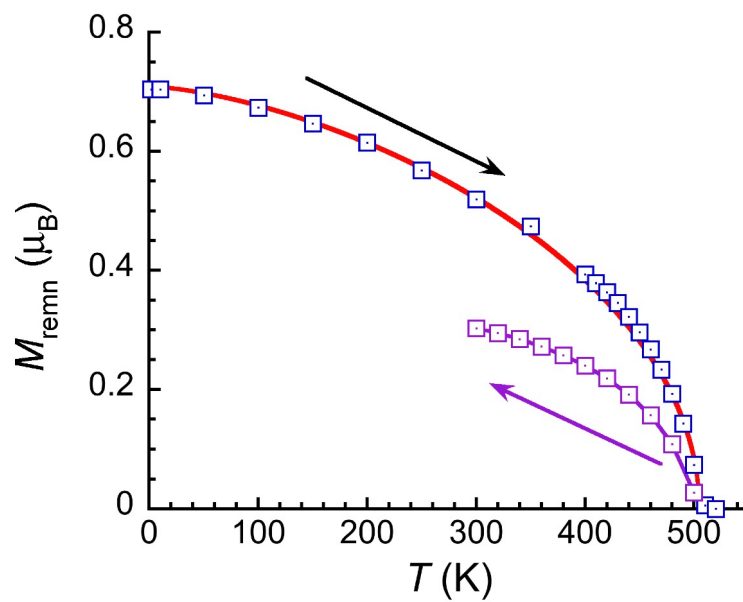
Fig. S29.

Temperature dependence of the remnant magnetization, M_{remn}, determined from the M vs. H data (Figs. 4B-C and S28) at each temperature for **2·(THF)** (and thus for **2·0.25(THF)** after partial desolvation above 400 K). The blue squares correspond to the first heating of the sample from 1.85 to 520 K, while the purple squares are determined upon cooling from 500 to 300 K. The solid red line is the best fit to the mean-field (MF) Bloch law: $M_{remn} \propto (1 - (T/T_{C\text{-}MF})^{3/2})^{1/2}$ with $T_{C\text{-}MF} = 506$ K, (considering data up to 490 K, $\chi^2(\text{GoF}) = 0.00057$; *42*). The solid purple line is a guide for the eye.

Fig. S30.
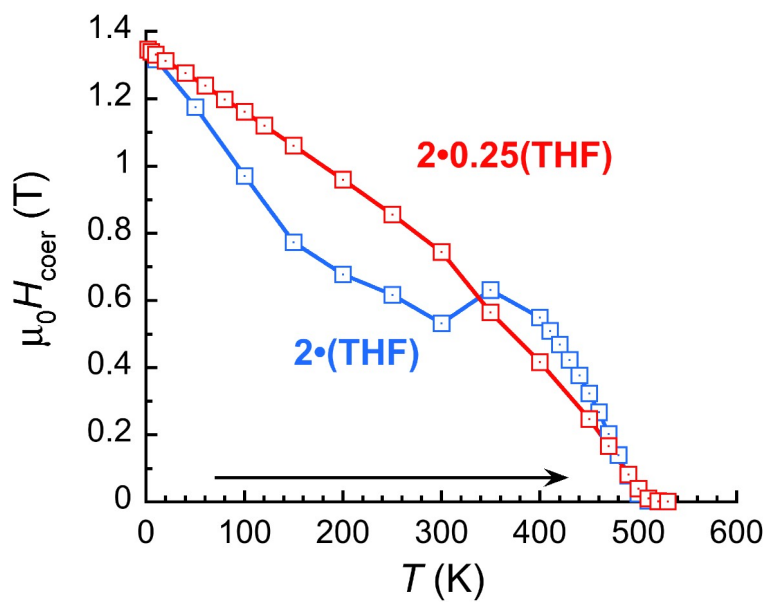
Temperature dependence of the coercive field, H_{coer}, determined at each temperature from the M vs. H data for **2·(THF)** (Figs. 4B-C; blue squares) and **2·0.25(THF)** (Fig. S31; red squares) on the first heating from 1.85 to 530 K. The solid lines are a guide for the eye.

Table S8.

Critical temperatures (T_C) and coercive fields (H_{Coer}) for commercial inorganic magnets, selected molecule-based magnets, **2•(THF)** and **2•0.25(THF)**.

	Compound	T_C (K)	RT H_{Coer} (Oe)	LT H_{Coer} (Oe)	Ref.
Inorganic magnets	Hard ferrites	720-735	1100-3100	H_{Coer} decreases upon cooling[*]	69
	AlNiCo₅	1130-1175	615-750	Not significantly sensitive to temperature[*]	69,70
	AlNiCo₈	1130	1500-1900		69
	SmCo₅	1000	6700-9000	43000 (4.2 K)[*]	69,70, 71
	Sm₂Co₁₇	1070	8000	15000-17000 (4.2 K)[*]	69,72
	Nd₂Fe₁₄B	550-590	9300-27000	50000-65000 (80 K)[*]	69,73
Molecule-based magnets	V[TCNE]$_x$·yCH₂Cl₂ ($x \sim 2$; $y \sim 0.5$)	> 350[†]	60	60 (4.2 K)	12,13
	V[TCNE]$_x$ ($x \sim 2$) thin films	400	~ 4.5	7 (5 K)	74
	V[Cr^{III}(CN)₆]₀.₈₆·2.8H₂O	315	≤ 25[‡]	25 (10 K)	23
	KV^{II}[Cr^{III}(CN)₆]·2H₂O	376	~ 4	165 (5 K)	75
	Polymerized TCNQ-linked covalent organic framework	> 400[‡]	~ 50	~ 300 (5 K)	24
	1,3,5-triazine-linked covalent organic framework	> 400[‡]	300	300 (10 K)	25
	Li₀.₇[Cr(pyz)₂]Cl₀.₇·(THF)	**510**	**5300**	**13500 (1.85 K)**	**this work**
	Li₀.₇[Cr(pyz)₂]Cl₀.₇·0.25(THF)	**515**	**7500**	**13500 (1.85 K)**	**this work**

RT: room temperature; LT: low temperature; TCNE: tetracyanoethylene; TCNQ: 7,7,8,8-tetracyanoquinodimethane

[*] The coercive fields for commercial inorganic magnets are strongly dependent on the sample preparation (heat treatment, grain size, surface impurities, doping…). The quoted values should thus be considered with caution as they are not necessarily intrinsic to the material.

[†] Above decomposition temperature.

[‡] Not experimentally reported.

Fig. S31.

Magnetization versus applied *dc* magnetic field data (at 5 to 12 Oe s^{-1}) in the -7 to 7 T field range for **2·0.25(THF)** from 1.85 K to 530 K.
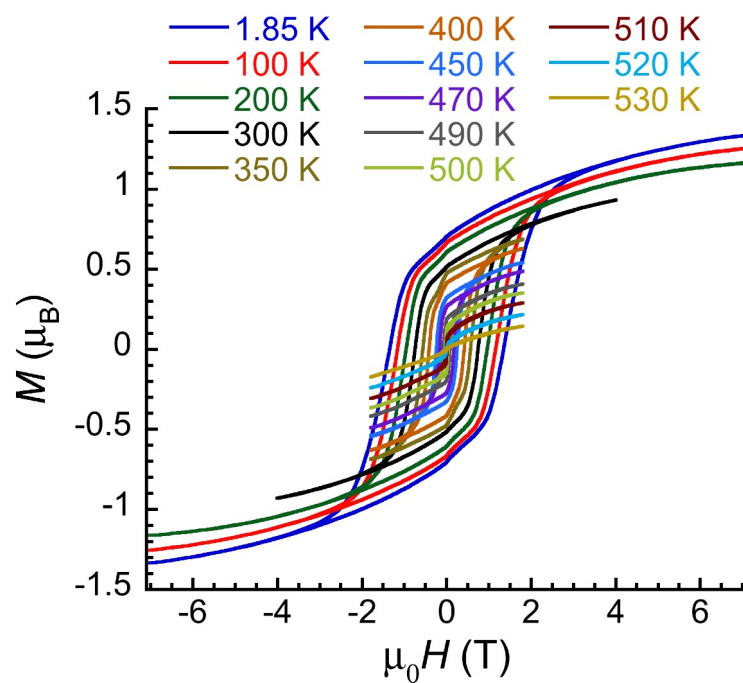
Fig. S32.

Magnified view of the magnetization versus applied *dc* magnetic field data (at 5 to 12 Oe s^{-1}) in the −2 to 2 T field range for **2·0.25(THF)** from 1.85 K to 530 K.
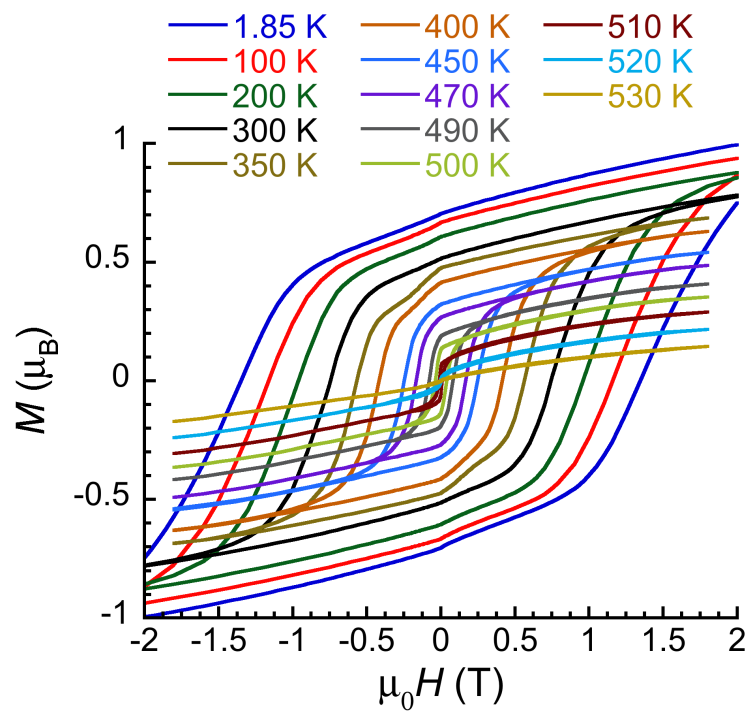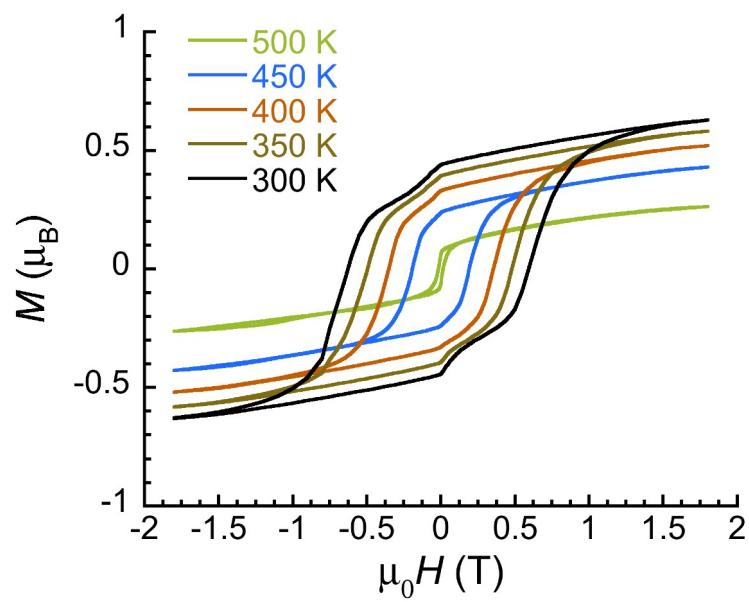
Fig. S33.

Magnetization versus applied *dc* magnetic field data (at 8 to 12 Oe s^{-1}) for **2·0.25(THF)** in the −1.8 to 1.8 T field range collected after the data shown in Figs. S31-S32 and decreasing the temperature from 500 to 300 K.
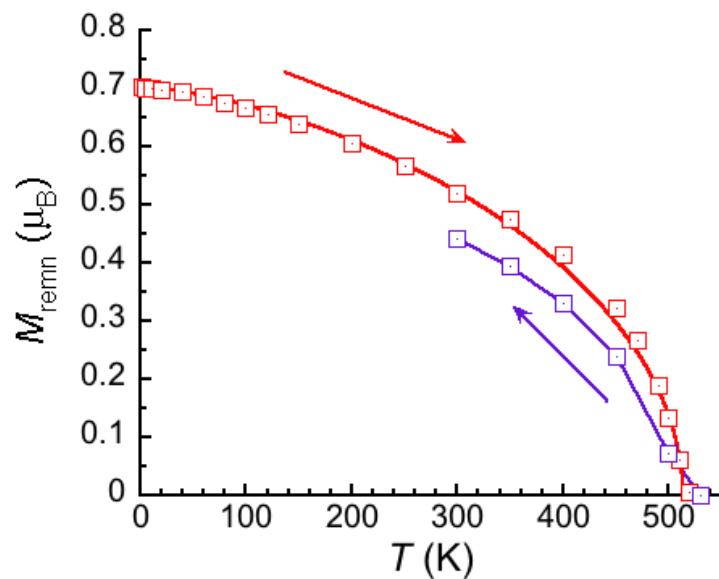
Fig. S34.

Temperature dependence of the remnant magnetization, M_{remn}, determined from the M vs. H data for **2·0.25(THF)** from 1.85 K to 530 K (Figs. S31-S32; red squares) and then on cooling down to 300 K (Fig. S33; purple squares). The solid red line is the best fit to the mean-field (MF) Bloch law: $M_{remn} \propto (1 - (T/T_{\text{C-MF}})^{3/2})^{1/2}$ with $T_{\text{C-MF}} = 514$ K, (considering data up to 510 K, $\chi^2(\text{GoF}) = 0.00195$; *42*). The solid purple line is a guide for the eye.
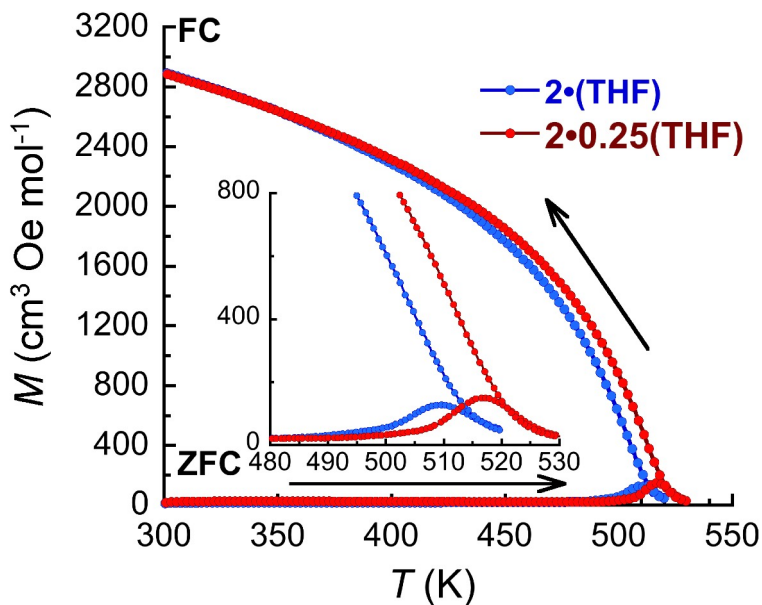
Fig. S35.

Zero-field cooled (ZFC)/field-cooled (FC) magnetization data for **2·(THF)** (blue) and **2·0.25(THF)** (red) obtained under an applied *dc* magnetic field of 50 Oe at 5 K min^{-1}. Inset: magnified view of the main plot in the temperature range 480-530 K. The samples were introduced first in the magnetometer at 300 K under zero field. Magnetization data were obtained while warming in 50 Oe (ZFC) and subsequently cooling (FC) to room-temperature under the same magnetic field. The solid lines are a guide for the eye.
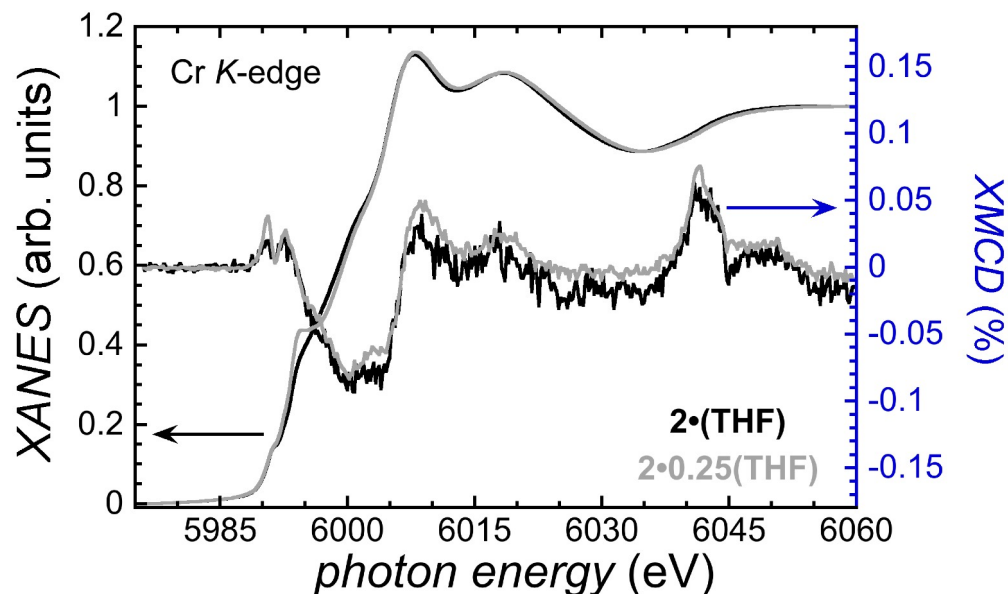
Fig. S36.

Normalized XANES and X-ray magnetic circular dichroism (XMCD) spectra at the Cr *K*-edge of **2·(THF)** (black line) and **2·0.25(THF)** (grey line) recorded at 295 K under 7-T applied magnetic field. XMCD spectra are given as the percentage of the XANES edge jump.[*]

[*]The Cr *K*-edge XMCD is able to measure the local chromium magnetization, as the spin-orbit interactions of the ligand atoms are negligibly small and consequently cannot introduce a significant orbital moment at the Cr centers (*26*). The above XMCD spectra for **2·(THF)** and **2·0.25(THF)** are essentially identical in shape and intensity (including Coster–Kronig multielectron excitations at 6040–6045 eV), unambiguously demonstrating the indistinguishable electronic and magnetic characteristics of Cr in the two materials.
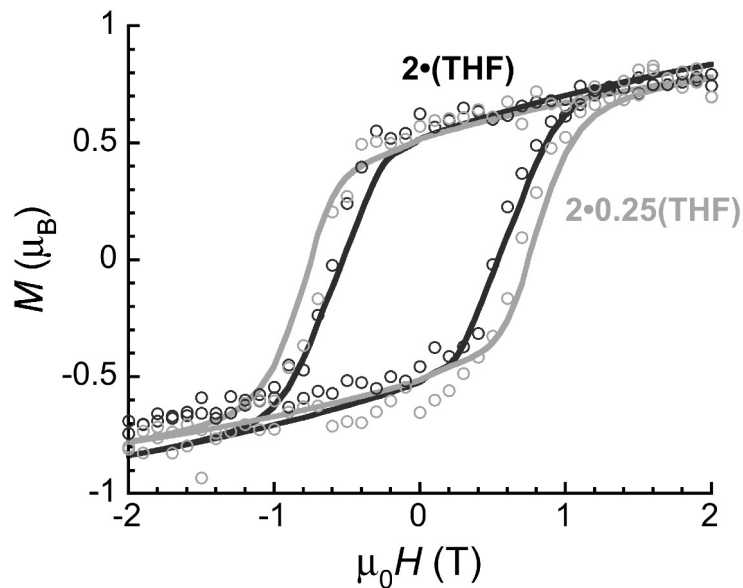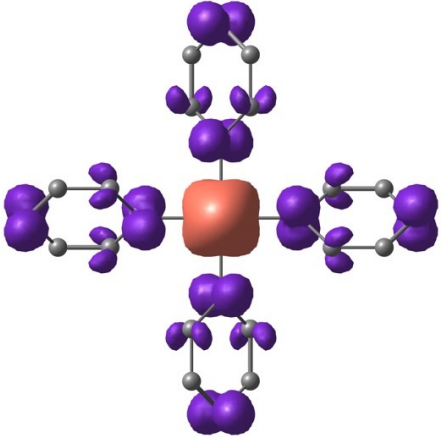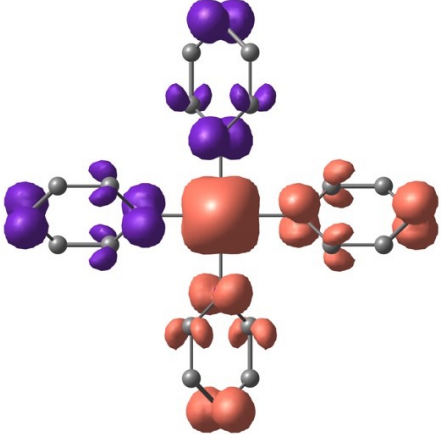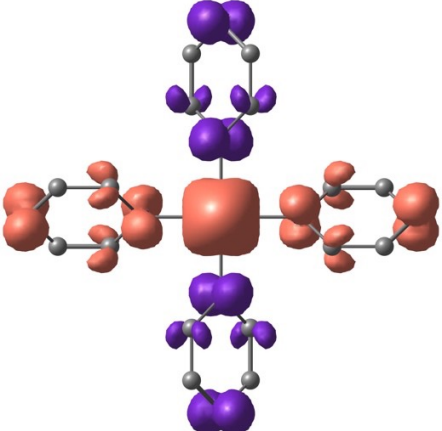
Fig. S37.
Field dependence of the XMCD signal (at $\approx$ 71 Oe s^{-1} and 295 K) at the maximum dichroism, 6000.7 eV, for **2·(THF)** (black circles) and **2·0.25(THF)** (grey circles) scaled and superimposed to the *M* vs. *H* data (at $\approx$ 5 Oe s^{-1}) at 300 K (black and grey solid lines, for **2·(THF)** and **2·0.25(THF)**, respectively). As expected, the field dependence of the local Cr magnetization is perfectly superimposed on the bulk *M* vs. *H* hysteresis loops, evidencing the dominant role of the Cr^{II} ions in the magnetic behavior of **2·(THF)** and **2·0.25(THF)**.

Table S9.

Calculated (B3LYP/def2-TZVP) energies of the high-spin state and three broken-symmetry states for the $[Cr(pyz)_4]^{2-}$ fragment extracted from the structural model of **2·0.25(THF)** used to calculate three exchange coupling constants using the Ising spin-Hamiltonian (Fig. S38). The spin density contour plots (0.01 isovalue) show which spins are flipped in a corresponding broken-symmetry state (purple color).

Energy (Hartree)	Spin Density (0.01 isovalue)
-2101.438322	
-2101.468333	
-2101.453861	
-2101.454293	
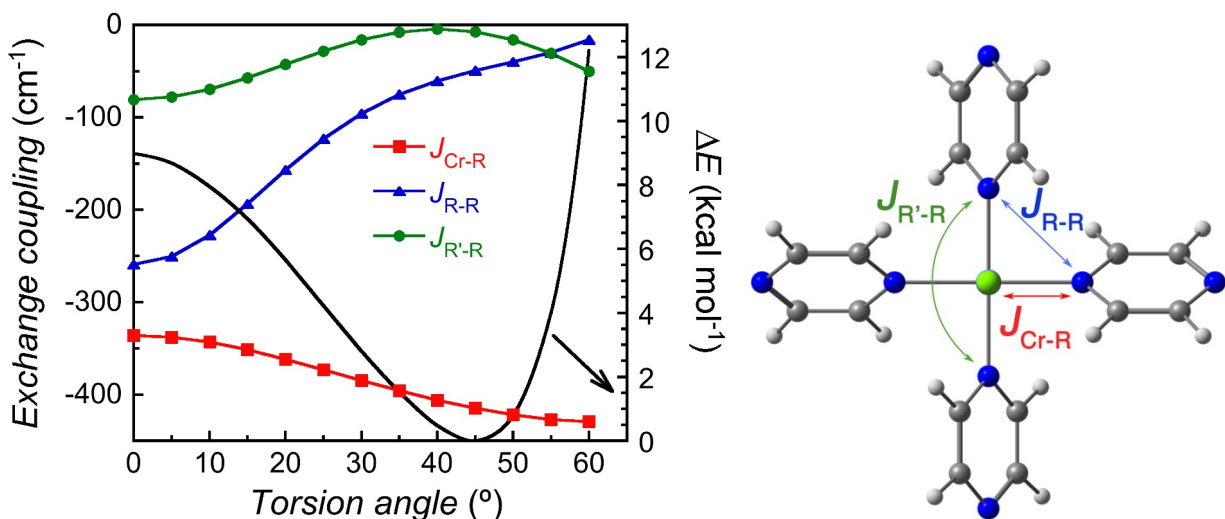
Fig. S38.

Left: Variation of the calculated (B3LYP/def2-TZVP) exchange coupling constants (in cm^{-1}; defined in the scheme on the right) for the $[Cr(pyz)_4]^{2-}$ fragment extracted from the structural model of **2·0.25(THF)** (Fig. 3) with a modified pyrazine torsion angle (the zero torsion angle corresponds to a perpendicular arrangement of all pyrazines with respect to the layer; experimentally the torsion angle is estimated at 43.2°). Difference in energy of the high-spin state at a given torsion angle relative to that at 45° (ΔE; in kcal mol^{-1}; see Table S10) is plotted as the black trace. The antiferromagnetic metal-ligand exchange interaction, $|J_{Cr-R}|$, increases by ~20% when the torsion angle changes from 0° and 60°. This effect is more pronounced for weaker exchange interactions between organic spins. Right: Scheme of the magnetic exchange pathways in the $[Cr(pyz)_4]^{2-}$ model fragment.

Table S10.

Variation of the exchange coupling constants (cm^{-1}; defined in the right part of Fig. S38), the associated high-spin state energy (absolute value, E in Hartree) and the difference in energy of the high-spin state at a given torsion angle relative to that at 45° (ΔE; in kcal mol^{-1}) with a modified pyrazine torsion angle (the zero angle corresponds to a perpendicular arrangement of all pyrazines with respect to the layer; the experimentally found torsion angle is 43.2°). These parameters were calculated for the [Cr(pyz)$_4$]$^{2-}$ fragment extracted from the structural model of **2·0.25(THF)** (Fig. 3).

Torsion angle (°)	Energy (Hartree)	J_{Cr-R}/hc (cm^{-1})	J_{R-R}/hc (cm^{-1})	$J_{R'-R}/hc$ (cm^{-1})	ΔE (kcal mol^{-1})
0	-2101.424124	-336	-259	-81	8.98
5	-2101.424599	-338	-251	-78	8.68
10	-2101.425758	-343	-227	-70	7.95
15	-2101.427372	-351	-194	-57	6.94
20	-2101.429411	-362	-157	-43	5.66
25	-2101.431694	-373	-123	-28	4.23
30	-2101.433952	-385	-96	-16	2.81
35	-2101.435989	-396	-75	-8	1.53
40	-2101.437674	-406	-60	-5	0.48
43.2	**-2101.438322**	**-412**	**-53**	**-6**	**0.07**
45	-2101.438434	-415	-49	-7	0.00
50	-2101.437174	-422	-40	-16	0.79
55	-2101.432058	-427	-30	-31	4.00
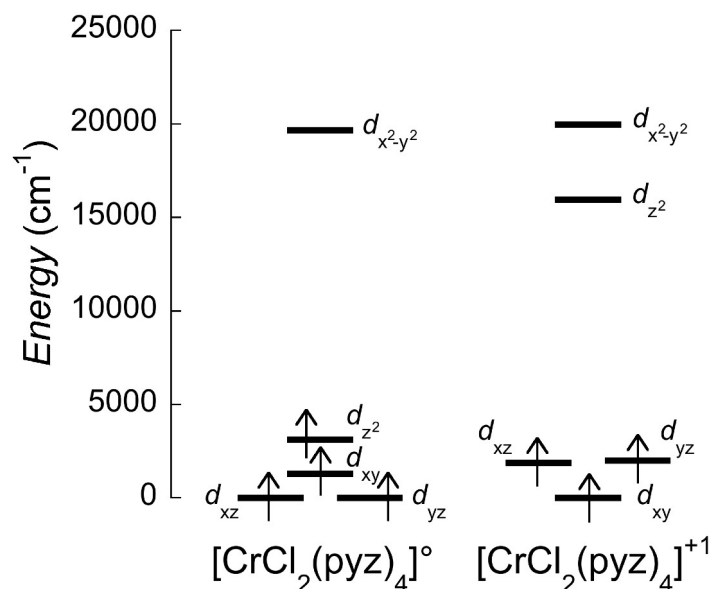
Fig. S39.

Ligand-field splitting of Cr $3d$ orbitals computed using *ab initio* ligand field theory based on CASSCF(4,5)/NEVPT2 calculations of a neutral $[Cr^{II}Cl_2(pyz)_4]°$ fragment from structural model of **2·0.25(THF)** (left) and a $[Cr^{III}Cl_2(pyz°)_4]^+$ fragment based on the X-ray structure of the $CrCl_2(pyz)_2$ precursor (right) (*26*). According to the calculations, the metal-ligand exchange interaction is strong and antiferromagnetic $J_{Cr-R}/hc = -412$ cm^{-1} (−593 K) in the $[Cr^{II}Cl_2(pyz)_4]^{4-}$ fragment for **2·0.25(THF)**, but this value is considerably smaller than in the $[Cr^{III}Cl_2(pyz)_4]°$ fragment for $CrCl_2(pyz)_2$ where the exchange interaction between Cr^{III} and the radical spin was estimated to be ~ −2000 cm^{-1} (*26*). The reason for that could be the additional contribution from singly occupied orbital (SOMO) d_{z2} of Cr^{II} in **2**, which is expected to be ferromagnetic due to its orthogonality with the SOMO of pyrazine radical.

References and notes

1. O. Gutfleisch, M. A. Willard, E. Brück, C. H. Chen, S. G. Sankar, J. P. Liu, Magnetic materials and devices for the 21st century: stronger, lighter, and more energy efficient. *Adv. Mater.* **23**, 821-842 (2011).
2. J. S. Miller, Organic- and molecule-based magnets. *Mater. Today* **17**, 224-235 (2014).
3. J. S. Miller, Magnetically ordered molecule-based materials. *Chem. Soc. Rev.* **40**, 3266-3296 (2011).
4. O. Kahn, *Molecular Magnetism* (VCH, Weinheim, 1993).
5. D. Gatteschi, R. Sessoli, J. Villain, *Molecular Nanomagnets* (Oxford University Press, 2006).
6. S. Demir, I.-R. Jeon, J. R. Long, T. D. Harris, Radical ligand-containing single-molecule magnets. *Coord. Chem. Rev.* **289-290**, 149-176 (2015).
7. C. Coulon, V. Pianet, M. Urdampilleta, R. Clérac, Single-Chain Magnets and Related Systems. In *Molecular Nanomagnets and Related Phenomena. Structure and Bonding,* S. Gao Eds. (Springer, Berlin, Heidelberg, 2014), vol. 164, pp. 143-184.
8. A. E. Thorarinsdottir, T. D. Harris, Metal-organic framework magnets. *Chem. Rev.* 10.1021/acs.chemrev.9b00666 (2020).
9. J. M. D. Coey, *Magnetism and Magnetic Materials* (Cambridge University Press, Cambridge, 2010).
10. N. Motokawa, H. Miyasaka, M. Yamashita, K. R. Dunbar, An electron-transfer ferromagnet with T_C = 107 K based on a three-dimensional [Ru$_2$]$_2$/TCNQ system. *Angew. Chem. Int. Ed.* **47**, 7760-7763 (2008).
11. X. Ma, E. A. Suturina, S. De, P. Négrier, M. Rouzières, R. Clérac, P. Dechambenoit, A redox-active bridging ligand to promote spin delocalization, high-spin complexes, and magnetic multi-switchability. *Angew. Chem. Int. Ed.* **57**, 7841-7845 (2018).
12. J. S. Miller, S.-I. Ohkoshi, High-T_C Ordered Molecular Magnets. In *Molecular Magnetic Materials: Concepts and Applications,* B. Sieklucka, D. Pinkowicz, Eds. (Wiley-VCH, 2017), chap. 7.
13. J. M. Manriquez, G. T. Yee, R. S. Mclean, A. J. Epstein, J. S. Miller, A room-temperature molecular/organic-based magnet. *Science* **252**, 1415-1417 (1991).
14. H. Liu, C. Zhang, H. Malissa, M. Groesbeck, M. Kavand, R. McLaughlin, S. Jamali, J. Hao, D. Sun, R. A. Davidson, L. Wojcik, J. S. Miller, C. Boehme, Z. V. Vardeny, Organic-based magnon spintronics. *Nat. Mater.* **17**, 308-312 (2018).
15. N. Zhu, X. Zhang, I. H. Froning, M. E. Flatté, E. Johnston-Halperin, H. X. Tang, Low loss spin wave resonances in organic-based ferrimagnet vanadium tetracyanoethylene thin films. *Appl. Phys. Lett.* **109**, 082402 (2016).
16. M. Chilcote, M. Harberts, B. Fuhrmann, K. Lehmann, Y. Lu, A. Franson, H. Yu, N. Zhu, H. Tang, G. Schmidt, E. Johnston-Halperin, Spin-wave confinement and coupling in organic-based magnetic nanostructures. *APL Mater.* **7**, 111108 (2019).
17. A. Franson, N. Zhu, S. Kurfman, M. Chilcote, D. R. Candido, K. S. Buchanan, M. E. Flatté, H. X. Tang, E. Johnston-Halperin, Low-damping ferromagnetic resonance in electron-beam patterned, high-Q vanadium tetracyanoethylene magnon cavities. *APL Mater.* **7**, 121113 (2019).
18. K. Taniguchi, J. Chen, Y. Sekine, H. Miyasaka, Magnetic phase switching in a tetraoxolene-bridged honeycomb ferrimagnet using a lithium ion battery system. *Chem. Mater.* **29**, 10053-10059 (2017).

19. L. Liu, J. A. DeGayner, L. Sun, D. Z. Zee, T. D. Harris, Reversible redox switching of magnetic order and electrical conductivity in a 2D manganese benzoquinoid framework. *Chem. Sci*. **10**, 4652-4661 (2019).

20. J. A. DeGayner, I.-R. Jeon, L. Sun, M. Dincă, T. D. Harris, 2D conductive iron-quinoid magnets ordering up to T = 105 K via heterogenous redox chemistry. *J. Am. Chem. Soc*. **139**, 4175-4184 (2017).

21. L. E. Darago, M. L. Aubrey, C. J. Yu, M. I. Gonzalez, J. R. Long, Electronic conductivity, ferrimagnetic ordering, and reductive insertion mediated by organic mixed-valence in a ferric semiquinoid metal-organic framework. *J. Am. Chem. Soc*. **137**, 15703-15711 (2015).

22. J. S. Miller, Oliver Kahn lecture: composition and structure of the V[TCNE]$_x$ (TCNE = tetracyanoethylene) room-temperature, organic-based magnet - a personal perspective. *Polyhedron* **28**, 1596-1605 (2009).

23. S. Ferlay, T. Mallah, R. Ouahès, P. Veillet, M. Verdaguer, A room-temperature organometallic magnet based on Prussian blue. *Nature* **378**, 701-703 (1995).

24. J. Mahmood, J. Park, D. Shin, H.-J. Choi, J.-M. Seo, J.-W. Yoo, J.-B. Baek, Organic ferromagnetism: trapping spins in the glassy state of an organic network structure. *Chem* **4**, 2357-2369 (2018).

25. H. Phan, T. S. Herng, D. Wang, X. Li, W. Zeng, J. Ding, K. P. Loh, A. T. S. Wee, J. Wu, Room-temperature magnets based on 1,3,5-triazine-linked porous organic radical frameworks. *Chem* **5**, 1223-1234 (2019).

26. K. S. Pedersen, P. Perlepe, M. L. Aubrey, D. N. Woodruff, S. E. Reyes-Lillo, A. Reinholdt, L. Voigt, Z. Li, K. Borup, M. Rouzières, D. Samohvalov, F. Wilhelm, A. Rogalev, J. B. Neaton, J. R. Long, R. Clérac, Formation of the layered conductive magnet CrCl$_2$(pyrazine)$_2$ through redox-active coordination chemistry. *Nat. Chem*. **10**, 1056-1061 (2018).

27. P. Perlepe, I. Oyarzabal, K. S. Pedersen, P. Negrier, D. Mondieig, M. Rouzières, E. A. Hillard, F. Wilhelm, A. Rogalev, E. A. Suturina, C. Mathonière, R. Clérac, Cr(pyrazine)$_2$(OSO$_2$CH$_3$)$_2$: a two-dimensional coordination polymer with an antiferromagnetic ground state. *Polyhedron* **153**, 248-253 (2018).

28. See supplementary materials.

29. T. Trella, W. Frank, poster presented at the 17. Conference of the GDCh Division of Solid State Chemistry and Materials Research, Dresden, DE, 15-17 September 2014.

30. Y.-F. Deng, T. Han, Z. Wang, Z. Ouyang, B. Yin, Z. Zheng, J. Krzystek, Y.-Z- Zheng, Uniaxial magnetic anisotropy of square-planar chromium(II) complexes revealed by magnetic and HF-EPR studies. *Chem. Commun*. **51**, 17688-17691 (2015).

31. S. Cuello, J. Entwisle, J. Benning, C. Liu, S. Coburn, K. G. McAdam, J. Braybrook, H. Goenaga-Infante, Complementary HPLC-ICP-MS and synchrotron X-ray absorption spectroscopy for speciation analysis of chromium in tobacco samples. *J. Anal. At. Spectrom*. **31**, 1818-1829 (2016).

32. E. Fawcett, Spin-density-wave antiferromagnetism in chromium. *Rev. Mod. Phys*. **60**, 209-283 (1988).

33. C. G. Shuli, M. K. Wilkinson, Neutron diffraction studies of various transition elements. *Rev. Mod. Phys*. **25**, 100-107 (1953).

34. G. E. Bacon, N. Cowlam, Magnetic studies of annealed and alloyed chromium by neutron diffraction. *J. Phys. C: Solid State Phys*. **2**, 238-251 (1969).

35. T. Furubayashi, I. Nakatani, Curie paramagnetism of chromium ultrafine particles. *J. Appl. Phys.* **73**, 6412-6413 (1993).

36. W. Abdul-Razzaq, M. S. Seehra, Observation of oxidation and mechanical strain in Cr nanoparticles produced by ball-milling. *Phys. Stat. Sol*. **193**, 94-102 (2002).

37. S. Foner, High-field antiferromagnetic resonance in Cr_2O_3. *Phys. Rev*. **130**, 183-197 (1963).

38. J. M. D. Coey, M. Venkatesan, Half-metallic ferromagnetism: example of CrO_2. *J. Appl. Phys*. **91**, 8345-8350 (2002).

39. S. DeBeer George, P. Brant, E. I. Solomon, Metal and ligand K-edge XAS of organotitanium complexes: metal 4p and 3d contributions to pre-edge intensity and their contributions to bonding. *J. Am. Chem. Soc*. **127**, 667-674 (2005).

40. A. B. Cairns, A. L. Goodwin, Structural disorder in molecular framework materials. *Chem. Soc. Rev*. **42**, 4881-4893 (2013).

41. T. N. Ramesh, R. S. Jayashree, P. V. Kamath, Disorder in layered hydroxides: DIFFaX simulation of the X-ray powder diffraction patterns of nickel hydroxide. *Clays Clay Miner*. **51**, 570-576 (2003).

42. R. Skomski, Permanent Magnets: History, Current Research, and Outlook. In *Novel Functional Magnetic Materials. Springer Series in Materials Science*, A. Zhukov Ed. (Springer Series in Materials Science, 2016), vol. 231, pp. 359-395.

43. F. Neese, Software update: the ORCA program system, version 4.0. *WIREs Comp. Mol. Sci*. **8**, e1327 (2018).

44. F. Neese, The ORCA program system. *WIREs Comp. Mol. Sci*. **2**, 73-78 (2012).

45. A. D. Becke, A new mixing of Hartree-Fock and local density-functional theories. *J. Chem. Phys*. **98**, 1372-1377 (1993).

46. C. Lee, W. Yang, R. G. Parr, Development of the Colle-Salvetti correlation-energy formula into a functional of the electron density. *Phys. Rev. B* **37**, 785-789 (1988).

47. S. H. Vosko, L. Wilk, M. Nusair, Accurate spin-dependent electron liquid correlation energies for local spin density calculations: a critical analysis. *Can. J. Phys*. **58**, 1200-1211 (1980).

48. P. J. Stephens, F. J. Devlin, C. F. Chabalowski, M. J. Frisch, Ab Initio calculation of vibrational absorption and circular dichroism spectra using density functional force fields. *J. Phys. Chem*. **98**, 11623-11627 (1994).

49. F. Weigend, R. Ahlrichs, Balanced basis sets of split valence, triple zeta valence and quadruple zeta valence quality for H to Rn: Design and assessment of accuracy. *Phys. Chem. Chem. Phys*. **7**, 3297-3305 (2005).

50. M. J. Frisch, G. W. Trucks, H. B. Schlegel, G. E. Scuseria, M. A. Robb, J. R. Cheeseman, G. Scalmani, V. Barone, G. A. Petersson, H. Nakatsuji, M. C. X. Li, A. Marenich, J. Bloino, B. G. Janesko, R. Gomperts, B. Mennucci, H. P. Hratchian, J. V. Ortiz, A. F. Izmaylov, J. L. Sonnenberg, D. Williams-Young, F. Ding, F. Lipparini, F. Egidi, J. Goings, B. Peng, A. Petrone, T. Henderson, D. Ranasinghe, V. G. Zakrzewski, N. R. J. Gao, G. Zheng, W. Liang, M. Hada, M. Ehara, K. Toyota, R. Fukuda, J. Hasegawa, M. Ishida, T. Nakajima, Y. Honda, O. Kitao, H. Nakai, T. Vreven, K. Throssell, J. A. M. Jr., J. E. Peralta, F. Ogliaro, M. Bearpark, J. J. Heyd, E. Brothers, K. N. Kudin, V. N. Staroverov, T. Keith, R. Kobayashi, J. Normand, K. Raghavachari, A. Rendell, J. C. Burant, S. S. Iyengar, J. Tomasi, M. Cossi, J. M. Millam, M. Klene, C. Adamo, R. Cammi, J. W. Ochterski, R. L. Martin, K. Morokuma, O. Farkas, J. B. Foresman, D. J. Fox, Gaussian, Revision D.01 (Gaussian, Inc., Wallingford, CT, 2016).

51. N. Lee, T. Petrenko, U. Bergmann, F. Neese, S. DeBeer, Probing valence orbital composition with iron k_β X-ray emission spectroscopy. *J. Am. Chem. Soc*. **132**, 9715-9727 (2010).

52. A. D. Becke, Density-functional exchange-energy approximation with correct asymptotic behavior. *Phys. Rev. A* **38**, 3098-3100 (1988).

53. J. P. Perdew, Density-functional approximation for the correlation energy of the inhomogeneous electron gas. *Phys. Rev. B* **33**, 8822-8824 (1986).
54. D. A. Pantazis, X.-Y. Chen, C. R. Landis, F. Neese, All-electron scalar relativistic basis sets for third-row transition metal atoms. *J. Chem. Theory Comput.* **4**, 908-919 (2008).
55. F. Neese, Efficient and accurate approximations to the molecular spin-orbit coupling operator and their use in molecular *g*-tensor calculations. *J. Chem. Phy.* **122**, 034107 (2005).
56. B. de Souza, G. Farias, F. Neese, R. Izsák, Predicting phosphorescence rates of light organic molecules using time-dependent density functional theory and the path integral approach to dynamics. *J. Chem. Theory Comput.* **15**, 1896-1904 (2019).
57. J. Rodríguez-Carvajal, Recent advances in magnetic structure determination by neutron powder diffraction. *Phys. B: Condens. Matter* **192**, 55-69 (1993).
58. M. S. Modeling, Materials Studio, version 5.5, http://accelrys.com/products/collaborative-science/biovia-materials-studio.
59. A. Rogalev, F. Wilhelm, Magnetic circular dichroism in the hard X-ray range. *Phys. Met. Metallogr.* **116**, 1285-1336 (2015).
60. A. Rogalev, V. Gotte, J. Goulon, C. Gauthier, J. Chavanne, P. Elleaume, XAFS and X-MCD spectroscopies with undulator gap scan. *J. Synchrotron Rad.* **5**, 989-991 (1998).
61. K. V. Klementiev, VIPER for Windows. Freeware: http:\\www.desy.de/~klmn/viper.html.
62. E. B. Wilson, The normal modes and frequencies of vibration of the regular plane hexagon model of the benzene molecule. *Phys Rev.* **45**, 706-714 (1934).
63. S. Breda, I. D. Reva, L. Lapinski, M. J. Nowak, R. Fausto, Infrared spectra pyrazine, pyrimidine and pyridazine in solid argon. *J. Mol. Struct.* **786**, 193-206 (2006).
64. K. V. Berezin, V. V. Nechaev, P. M. El'kin, Anharmonic resonances in the vibrational spectra of pyrazine. *J. Appl. Spectrosc.* **72**, 9-19 (2005).
65. J. F. Arenas, M. S. Woolley, I. L. Tocón, J. C. Otero, J. I. Marcos, Complete analysis of the surface-enhanced Raman scattering of pyrazine on the silver electrode on the basis of a resonant charge transfer mechanism involving three states. *J. Chem. Phys.* **112**, 7669-7683 (2000).
66. A. C. González-Baró, R. Pis-Diez, O. E. Piro, B. S. Parajón-Costa, Crystal structures, theoretical calculations, spectroscopic and electrochemical properties of Cr(III) complexes with dipicolinic acid and 1,10-phenantroline, *Polyhedron* **27**, 502-512 (2008).
67. B. Cadioli, E. Gallinella, C. Coulombeau, H. Jobic, G. Berthier, Geometric structure and vibrational spectrum of tetrahydrofuran. *J. Phys. Chem.* **97**, 7844-7856 (1993).
68. H. F. Shurvell, M. C. Southby, Infrared and Raman spectra of tetrahydrofuran hydroperoxide. *Vib. Spectrosc*. **15**, 137-146 (1997).
69. F. Cardarelli, Magnetic Materials. In *Materials Handbook: A Concise Desktop Reference* (Springer-Verlag, London Ltd, ed. 2, 2008), pp. 510-517.
70. M. S. Walmer, C. H. Chen, M. H. Walmer, A New Class of Sm-TM Magnets for Operating Temperatures Up to 550°C. *IEEE Trans. Magn.* **36**, 3376-3381 (2000)
71. R. Kütterer, H.- R. Hilzinger, H. Kronmüller, The temperature dependence of the coercive field of Co_5Sm magnets. *J. Magn. Magn. Mater.* **4**, 1-7 (1977).
72. J. C. Téllez-Blanco, X. C. Kou, R. Grössinger, E. Estévez-Rams, J. Fidler, B M. Ma, Coercivity and magnetic anisotropy of sintered Sm_2Co_{17}-type permanent magnets. *J. App. Phys.* **82**, 3928-3933 (1997).

73. C. Benabderrahmane, N. Béchu, P. Berteaud, M. E. Couprie, J. M. Filhol, C. Herbeaux, C. Kitegi, J. L. Marlats, K. Tavakoli, A. Mary, *Proceedings of the 11th European Particle Accelerator Conference*, Genoa, Italy, 23-27 June 2008, 2225-2227 (2008).

74. K. I. Pokhodnya, A. J. Epstein, J. S. Miller, Thin-Film $V[TCNE]_x$ Magnets. *Adv. Mater.* **12**, 410-413 (2000).

75. S. M. Holmes, G. S. Girolami, Sol-Gel Synthesis of $KV^{II}[Cr^{III}(CN)_6] \cdot 2H_2O$: A Crystalline Molecule-Based Magnet with a Magnetic Ordering Temperature above 100°C. *J. Am. Chem. Soc.* **121**, 5593-5594 (1999).